

THE SIZE EVOLUTION OF GALAXIES SINCE Z~3: COMBINING SDSS, GEMS AND FIRES¹

IGNACIO TRUJILLO², NATASCHA M. FÖRSTER SCHREIBER³, GREGORY RUDNICK^{4,10}, MARCO BARDEN², MARIJN FRANX⁵, HANS-WALTER RIX², J. A. R. CALDWELL⁶, DANIEL H. MCINTOSH⁷, ANDREW ZIRM⁵, BORIS HÄUSSLER², PIETER G. VAN DOKKUM⁹, IVO LABBÉ^{5,11}, ALAN MOORWOOD⁸, HUUB RÖTTGERING⁵, ARJEN VAN DER WEL⁵, PAUL VAN DER WERF⁵, LOTTIE VAN STARKENBURG⁵

Draft version February 7, 2020

ABSTRACT

We present the evolution of the luminosity-size and stellar mass-size relations of luminous ($L_V \gtrsim 3.4 \times 10^{10} h_{70}^{-2} L_\odot$) and of massive ($M_* \gtrsim 3 \times 10^{10} h_{70}^{-2} M_\odot$) galaxies in the last ~ 11 Gyr. We use very deep near-infrared images of the Hubble Deep Field-South and the MS1054-03 field in the J_s , H and K_s bands from FIRES to retrieve the sizes in the optical rest-frame for galaxies with $z > 1$. We combine our results with those from GEMS at $0.2 < z < 1$ and SDSS at $z \sim 0.1$ to achieve a comprehensive picture of the optical rest-frame size evolution from $z=0$ to $z=3$. Galaxies are differentiated according to their light concentration using the Sérsic index n . For less concentrated or disk-like objects ($n \lesssim 2$), the galaxies at a given luminosity were typically ~ 2.3 times smaller at $z \sim 2.5$ than those we see today. The stellar mass-size relation has evolved significantly less: the mean size at a given stellar mass was ~ 1.5 times smaller at $z \sim 2.5$. Simple scaling relations between dark matter halos and baryons in a hierarchical cosmogony predict a stronger than observed evolution of the stellar mass-size relation. The observed luminosity-size evolution out to $z \sim 1.7$ matches well recent infall model predictions for Milky-Way type objects. For disk galaxies, the weak redshift-dependence of the stellar mass-size relation would follow naturally if the individual galaxies grow inside-out, evolving “along” the relation. For highly concentrated or spheroid-like objects ($n \gtrsim 2$), the situation is similar to the disk-like objects: at a given luminosity, these galaxies were ~ 2.9 times smaller at $z \sim 2.5$ (or put differently, were typically ~ 2.3 mag brighter at a given size than they are today), and at a given stellar mass the size has evolved slightly (a factor of 1.4). This result is consistent with passive evolution of the stellar population of these galaxies. However, for the most massive ($M_* \gtrsim 6.6 \times 10^{10} h_{70}^{-2} M_\odot$) spheroid-like objects at $z > 1.4$ in our sample there is a hint that they were ~ 2 times smaller than present-day early-type galaxies of the same mass.

Subject headings: galaxies: fundamental parameters, galaxies: evolution, galaxies: high redshift, galaxies: structure

1. INTRODUCTION

Over the last decades (starting with Fall & Efstathiou 1980) there has been a substantial effort on understanding, theoretically and through observations, how galaxies have reached their current sizes over cosmic time. The answer to this question plays a key role in our understanding of galaxy formation and evolution.

Several approaches have been tried to make specific predictions about how the size of the galaxies (particularly the disk galaxies) evolves with redshift: the semi-analytical hierarchi-

¹ Based on observations collected at the European Southern Observatory, Paranal, Chile (ESO LP 164.O-0612). Also, based on observations with the NASA/ESA *Hubble Space Telescope*, obtained at the Space Telescope Science Institute, which is operated by AURA Inc, under NASA contract NAS 5-26555.

² Max-Planck-Institut für Astronomie, Königstuhl 17, 69117 Heidelberg, Germany

³ Max-Planck-Institut für extraterrestrische Physik, Giessenbachstrasse, D-85748, Garching, Germany

⁴ Max-Planck-Institut für Astrophysik, Postfach 1317, D-85748, Garching, Germany

⁵ Leiden Observatory, P.O. Box 9513, NL-2300 RA, Leiden, The Netherlands

⁶ University of Texas, McDonald Observatory, Fort Davis, TX 79734

⁷ Astronomy Department, University of Massachusetts, 710 N. Pleasant St., Amherst, MA 01003

⁸ European Southern Observatory, D-85748, Garching, Germany

⁹ Department of Astronomy, Yale University, P.O. Box 208101, New Haven, CT 06520-8101

¹⁰ Present Address: NOAO, 950 N. Cherry Av. Tucson AZ 85719

¹¹ Present Address: Carnegie Observatories, 813 Santa Barbara Street, Pasadena, CA 91101

cal models, direct numerical simulations and infall models.

The semi-analytical hierarchical model assumes simple scaling relationships between the properties of the galaxy disks and the halos in which they live (Fall & Efstathiou 1980; Dalcanton et al. 1997; Mo, Mao & White 1998; van den Bosch 2000). According to this picture, galaxy disks are formed from gas with some initial angular momentum that cools and contracts in dark matter halos. The mass and the angular momentum that settle in the disk are some fixed fractions of the mass and the angular momentum of the halo respectively. The mass and size of the halos are tightly linked to the density of the universe at the time the halos were formed; consequently, halos formed at high- z are expected to be much denser than halos formed at lower z . Under the assumption that the disk mass and angular momentum fractions together with the spin parameter of the halo do not vary with redshift, Mo et al. suggest the following redshift scaling for the size of the baryonic disk at their *formation* redshift: $R \propto H^{-1}(z)$ at a fixed circular halo velocity or $R \propto H^{-2/3}(z)$ at a fixed halo mass, where $H(z)$ is the Hubble constant at a given z : $H(z) = H_0 [\Omega_m (1+z)^3 + \Omega_\Lambda]^{1/2}$ in a flat Universe.

High-resolution N-body/gas-dynamical simulations (see e.g. Navarro & Steinmetz 2000) find that the above picture is too simplistic; e.g. large systematic variations in the fraction of baryons that collapse to form galaxies are observed and angular momentum conservation may not hold. Moreover, the explanation of the observed local size-mass relation within this hierarchical context (Shen et al. 2003) requires that the above scaling between the dark matter and baryons is

broken and instead that the fraction of baryons in the disk is a function of the halo mass. This is also predicted by standard feedback models based on galactic winds.

The infall model approach (Cayón, Silk & Charlot 1996; Bouwens, Cayón & Silk 1997) examines a number of local disk galaxies in great detail and uses detailed models of their observed properties, e.g. gas profiles, stellar profiles, metallicity profiles, current star formation rate (SFR), and age–metallicity relationships, to infer how galaxies might have evolved to high redshift. This approach uses the local universe as a reference and consequently does not explain why the local galaxy population is as it is. The main ingredients of these models are: a) that the SFR is determined at each radius and time from the local gas density according to a Schmidt–type law, and b) that metal–free gas infalls with certain time-scale. Using the Milky Way as reference, Bouwens & Silk (2002) provide the following size scaling relationship with redshift: $R(z)/R(0)=1-0.27z$.

In the case of spheroid–dominated galaxies, they are expected to form from the merging of smaller systems (White & Frenk 1991) and consequently to have a different size evolution than disk–dominated systems. The old stellar populations found in nearby ellipticals make it unlikely that these galaxies were the remnant of a merger between two similar spirals drawn from the observed local population. In fact, Khochfar & Burkert (2003) have shown that dissipationless mergers of early–type galaxies may dominate the formation of the nowadays high–mass early–type galaxies. Shen et al. (2003) have shown that the present–day stellar mass–size relation for early–type galaxies follows $R \propto M^{0.56}$. Shen et al. indicate that the present–day relation is consistent with a model where early–type galaxies are the remnants of repeated mergers where the progenitors have properties similar to those of faint ellipticals. According to their model, the size of the remnant increases after each merger. In this context, we would expect that early–type galaxies that have undergone a major merger were larger in size than galaxies of the same mass that have not suffered such a process.

Detailed modeling of the merger histories of galaxies in the cold dark matter scenario suggests that the last major merging event is typically around redshift unity (Kauffmann & Haehnelt 2000). Consequently, we would expect that the sizes of early–type galaxies at $z>1$ were, in general, smaller than the local counterparts. An analysis of the evolution of the stellar mass–size relation at high– z of these objects can restrict the above scenario of merging formation.

Historically, the monolithic collapse scenario (Eggen, Lynden–Bell & Sandage 1962; Larson 1975) envisioned that all spheroidal galaxies formed very early via a rapid collapse of the gas at high redshift. In this picture, E/S0 would be already in place at high– z and we would expect then that the changes in the observed properties of early–type galaxies over time were due to simple passive fading of their stellar populations. The more modern version of this scenario envisions that also massive ellipticals formed hierarchically, but at quite high redshift.

The evolution of individual galaxies is not directly observable. However, look–back studies can provide extensive information on how the population properties of galaxies have changed with cosmic epoch. Early studies (Smail et al. 1995; Casertano et al. 1995; Roche et al. 1998) showed that galaxies at a given luminosity were smaller in the past. However, it was not until the application of the Lyman–break technique (Steidel et al. 1996) that the study of a large number of galaxies

at high– z universe was possible. This technique is specially efficient at selecting star–forming galaxies at $z>2$. Sizes have been measured for these Lyman Break Galaxies (LBGs) (Giavalisco, Steidel & Macchetto 1996; Lowenthal et al. 1997; Ferguson et al. 2004), but using optical filters, i.e. measuring their sizes in the rest–frame ultra–violet (UV) region of their spectra. At these wavelengths the LBGs appear compact ($r \sim 0.^{\circ}2-0.^{\circ}3$, $\sim 1.5-2.5 h_{70}^{-1}$ kpc). However, there is some evidence that the LBG morphology depends not much on the wavelength, remaining essentially unchanged from the far–UV to the optical window (Giavalisco 2002 and references therein).

As a result of the dearth of very deep near–infrared (NIR) images, most of the studies using the rest–frame optical have been limited in redshift up to $z \sim 1$ (Lilly et al. 1998; Simard et al. 1999; Ravindranath et al. 2004; Trujillo & Aguerri 2004; McIntosh et al. 2005; Barden et al. 2005). To properly compare with local optically selected samples and to trace the size evolution in a consistent fashion at $z>1$ one needs to use very deep NIR data. On doing that any observed size evolution would then reflect true evolutionary changes not subject to the changing appearance of galaxies in different bandpasses. Moreover, it seems now clear that rest–frame UV selected samples do not provide a complete census of the galaxy population at high– z (e.g. Franx et al. 2003; van Dokkum et al. 2003; Daddi et al. 2004) and, in particular, a substantial population of red objects are missing from purely rest–frame UV selected surveys.

In addition to the use of rest–frame optical sizes, it would be of great help to facilitate a direct comparison with the theoretical expectations if the size evolution could be measured at a given mass rather than a given luminosity. Using circular velocity measurements to estimate galaxy masses at high– z is extremely difficult and very few objects have been analyzed (see e.g. Vogt et al. 1996; 1997). An alternative approach is to estimate the stellar masses from their rest–frame colors and spectral energy distributions (SEDs).

With the above ideas in mind we performed an exploratory work (Trujillo et al. 2004) to probe the evolution of the luminosity–size and stellar mass–size relations of the galaxies out to $z \sim 3$. That work used very deep NIR images of the Hubble Deep Field–South (HDF–S) from the Faint Infrared Extragalactic Survey (FIRES; Franx et al. 2000). We found that the rest–frame V–band sizes of luminous galaxies ($\langle L_V \rangle \sim 4 \times 10^{10} h_{70}^{-2} L_\odot$) at $2 < z < 3$ were 3 times smaller than for equally luminous galaxies today. In contrast, the mass–size relation had evolved relatively little: the size at mass ($\langle M_* \rangle \sim 4 \times 10^{10} h_{70}^{-2} M_\odot$), had changed by 20% ($\pm 20\%$) since $z \sim 2.5$.

In the present work we add to the above data set the results from the analysis of the ~ 4 times larger MS1054–03 FIRES field. Using both FIRES fields we decrease the effects of the field–to–field variations in our results and multiply by three the number of objects with $z>1$ in our sample. In addition, we make a detailed comparison of our results with those found in the Sloan Digital Sky Survey (SDSS; York et al. 2000) at $z \sim 0.1$ and in the Galaxy Evolution from Morphology and SEDs (GEMS; Rix et al. 2004) survey at intermediate redshift $0.2 < z < 1$. This allows us to follow in detail the evolution of the luminosity–size and stellar mass–size relations of the luminous galaxies over the last ~ 11 Gyr.

The structure of this paper is as follows. In Sect. 2 we describe the FIRES data, and in Sect. 3 the size measurement technique and robustness estimations for the FIRES data. In

Sect. 4 we present the observed luminosity–size and stellar mass–size relations and compare our results with other samples in Sect. 5. We discuss our results in Sect. 6.

All magnitudes in this paper are given in the AB system unless otherwise stated. Throughout, we will assume a flat Λ –dominated cosmology ($\Omega_M=0.3$, $\Omega_\Lambda=0.7$ and $H_0=70 \text{ km s}^{-1} \text{ Mpc}^{-1}$).

2. FIRES: DATA

The data used here were obtained as part of FIRES (Franx et al. 2000), a non–proprietary NIR survey of the HDF–S and MS 1054–03 fields carried out at the European Southern Observatory (ESO) Very Large Telescope (VLT). The data processing and photometry are discussed in detail by Labb   et al. (2003a) for HDF–S and F  rster Schreiber et al. (2005; in preparation) for the MS 1054–03 field¹².

The NIR images were obtained using the VLT Infrared Spectrograph And Array Camera (ISAAC; Moorwood et al. 1997). The HDF–S was imaged for 33.6 hr in J_s , 32.3 hr in H , and 35.6 hr in K_s in a single $2.5' \times 2.5'$ pointing covering the Hubble Space Telescope (HST) WFPC2 main field. The NIR data were complemented with deep optical publicly available HST WFPC2 imaging in the U_{300} , B_{450} , V_{606} and I_{814} bands (Casertano et al. 2000). For the MS 1054–03 field, 77 hr of ISAAC integration time was obtained in a $5' \times 5'$ mosaic of four pointings. Already existing mosaics in the WFPC2 V_{606} and I_{814} bands (van Dokkum et al. 2000) were used. In addition, Bessel U, B, and V band imaging with the VLT FORS1 instrument were collected.

The depth (3σ) reached was 26.8 mag in J_s , 26.2 mag in H , and 26.2 mag in K_s for point sources in the HDF–S. The MS 1054–03 field surveys an area four times larger down to ~ 0.7 mag brighter magnitudes. The effective seeing in the reduced images is approximately $0.47'$ in all NIR bands in the HDF–S and $0.49'$ in the MS 1054–03 field.

The sources were selected in the K_s band using version 2.2.2 of the SExtractor software (Bertin & Arnouts 1996). K band selected samples assure, for $z \lesssim 3$ galaxies, a selection based on flux at wavelengths redder than the rest–frame V band. This selection is less sensitive to the current unobscured star formation rate than selections based in the rest–frame UV bands. From the above K band catalogs we removed stars if their spectral energy distributions (SEDs) were better fitted by a single stellar template than by a linear combination of galaxy templates. In the HDF–S two obviously extended objects were removed from the star lists and in MS1054–03 field, 4 bright spectroscopically identified stars were added to the star lists.

Photometric redshifts z_{ph} , as well as the rest–frame optical luminosities, were estimated by fitting a linear combination of redshifted SEDs of galaxies of various types (Rudnick et al. 2001, 2003). Comparison with available spectroscopic redshifts z_{sp} implies an accuracy of $\delta z \equiv |z_{sp} - z_{ph}| / (1 + z_{sp}) \geq 0.074$ for both fields. When possible, spectroscopic redshifts were used.

To ensure sufficient signal–to–noise ratio for the subsequent size determinations we selected only galaxies with $K_s \leq 23.5$ in the HDF–S and $K_s \leq 23$ in the MS 1054–03 field and whose fractional exposure time in all the filters were larger than 15% of the maximum in each field. This leaves us with a total sample of 171 objects in the HDF–S and 708 in the MS 1054–03

¹² The reduced images, photometric catalogs, photometric redshift estimates, and rest–frame luminosities are available online through the FIRES home page at <http://www.strw.leidenuniv.nl/~fires>.

field. The large number of objects in the MS 1054–03 field is caused by a “foreground” cluster at $z=0.83$. To avoid possible contamination in our field galaxy analysis by cluster galaxies we only select objects with $z \geq 1$. This is particularly effective at bright magnitudes due to the high spectroscopic completeness for cluster members. For homogeneity, the same z cut is used in the HDF–S in the present work.

The final number of galaxies used in this paper is 87 in the HDF–S and 175 in the MS 1054–03 field.

The stellar mass–to–light (M/L) ratio and hence the stellar masses of the objects are estimated by Rudnick et al (2005, in preparation), using rest–frame (B–V) color and SEDs similar to that of Bell & de Jong (2001). We use the relation between color and M/L, which exists over a wide range of monotonic star formation histories and is rather robust against the effects of age, dust extinction, or metallicity. The largest systematic errors in the derived stellar mass will occur for galaxies with strong ongoing bursts.

3. FIRES: REST–FRAME SIZE ESTIMATIONS

The galaxy sizes used in this paper are measured in the observed band that is closest to the rest–frame V–band at every redshift; this means J_s for galaxies with $1 < z < 1.5$, H for galaxies with $1.5 < z < 2.6$ and K_s for galaxies with $2.6 < z < 3.2$. In addition, we have also measured the sizes of all our galaxies in the K_s band to analyze the completeness of the sample and test the robustness of the retrieved structural parameters. The structural properties of the galaxies are estimated from a S  rsic’s (1968) $r^{1/n}$ model, convolved with the image point–spread function (PSF). The PSF was estimated for every band by fitting a Moffat function to star profiles. We find that this analytical PSF represents very accurately the stars profiles. Best–fitting stellar parameters are summarized in the Table 1. The S  rsic model is given by

$$I(r) = I(0) \exp \left[-b_n \left(\frac{r}{r_e} \right)^{1/n} \right], \quad (1)$$

where $I(0)$ is the central intensity and r_e the effective radius enclosing half of the flux from the model light profile. The quantity b_n is a function of the radial shape parameter n – which defines the global curvature in the luminosity profile – and is obtained by solving the expression $\Gamma(2n)=2\gamma(2n, b_n)$, where $\Gamma(a)$ and $\gamma(a, x)$ are respectively the gamma function and the incomplete gamma function.

The S  rsic model is a flexible parametric description of the surface brightness distribution of the galaxies and contains the exponential ($n=1$) and de Vaucouleurs ($n=4$) models as particular cases. In addition, this model is used in the structural analysis of the SDSS galaxy sample (our local comparison sample; Blanton et al. 2003; Shen et al. 2003) and the GEMS data (our comparison sample for galaxies in the redshift range $0.2 < z < 1$; Barden et al. 2005; McIntosh et al. 2005).

The details of the fitting procedure, as well as examples of profile fitting, are shown in Trujillo et al. (2004) and references therein. A Levenberg–Marquardt non–linear fitting algorithm (Press et al. 1992) was used to determine the set of free parameters which minimizes χ^2 . A variety of starting parameters are used to ensure that our fits do not get trapped in local χ^2 minima. Our code has already been used and tested in a variety of HST and ground–based studies of nearby and distant galaxies (see Trujillo & Aguerri 2004 for references).

Comparisons with other fitting codes have already been done: GALFIT (Peng et al. 2002) in Trujillo et al. (2004) and

TABLE 1
MOFFAT PSF FIT TO THE SAMPLE
IMAGES

Filter	β	FWHM
HDF-S		
J_s	3	0''.46
H	3	0''.49
K_s	3	0''.47
MS 1054-03		
J_s	3.5	0''.48
H	3	0''.46
K_s	3	0''.53

NOTE. — Col. (1): Filters used. Col. (2) and Col. (3) β and FWHM values estimated by fitting a Moffat PSF to star profiles in the NIR images.

GIM2D (Simard 1998) in Trujillo & Aguerri (2004), finding a good agreement (at the 35% (1σ) level) in the recovered structural parameters. In what follows, we refer to the “circularized effective radius” of the fitted model, i. e., $r_e = a_e \sqrt{1 - \epsilon}$, where a_e is the semimajor effective radius (directly measured in our fits) and ϵ the intrinsic (non-seeing affected) projected ellipticity of the galaxy. The results of our fitting are shown in Table 4 for the MS1054-03 data. The HDF-S data is given in Trujillo et al. (2004). There are 7 objects with $z > 1$ in our full sample (ID: MS73, MS914, MS1114, MS1265, MS1356, MS1410, MS1717) whose effective radius is $\sim 0''.1$ (i.e. equal or very close to the pixel size of our images). These objects look very compact and could be AGNs. For the brightest object, MS1356, where spectroscopic analysis has been made (van Dokkum et al. 2003; 2004) this is confirmed. For that reason, because their sizes could be not indicative of the sizes of their host galaxies these objects are not considered throughout.

3.1. Structural Parameter Estimates

3.1.1. Simulations

The results presented in this paper rely on our ability to measure accurate structural parameters. To gauge the accuracy of our parameter determination we have created 300 artificial galaxies uniformly generated at random in the following ranges: $20 \leq K_s(AB) \leq 23$, $0''.1 \leq r_e \leq 1''.2$, $0.5 \leq n \leq 6$ and $0 \leq \epsilon \leq 0.8$. The mock galaxies are created using the IRAF tasks MKOBJECT and FCONVOLVE, using a large number of subpixels per image pixel to allow accurate convolutions between the PSF and the galaxy surface brightness distribution models. To simulate the real conditions of our observations, we add a background sky image (free of sources) taken from a piece of the MS1054 field image in the K_s band. To match the observations, the PSF FWHM in the simulation was set at $0''.53$ (i.e. we used the K_s -band PSF of the MS1054 field, our worst seeing case). The same procedure was used to retrieve the structural parameters both in the simulated and actual images.

The results of these simulations are shown in Figs. 1 and 2. Towards fainter apparent magnitude the parameters recovered are systematically worse. At increasing magnitude the code recovers systematically lower sizes and Sérsic indexes. The bias depends strongly on the shape of the surface brightness profiles. We illustrate this by separating the galaxies between

less light concentrated profiles ($n < 2$) and highly concentrated profiles ($n > 2$). Galaxies with larger n are more biased than those with lower values. The reason is that, at a given magnitude, galaxies with larger n have a surface brightness profile which decreases faster and is, consequently, sooner affected by the noise. The size of the galaxies plays also a role at determining the bias on the structural parameters: at a given magnitude, larger galaxies are slightly more biased than smaller ones towards shorter sizes, however, the shapes are recovered slightly better at larger sizes.

To illustrate the magnitude of the biases in the different parameters we summarize the results for the most affected bin, $K_s = 22.5$ mag. For galaxies with $n < 2$ we find the following systematics: $8(\pm 14)\%$ lower luminosities, $18(\pm 17)\%$ lower sizes, $29(\pm 22)\%$ lower Sérsic indices. For galaxies with $n > 2$: $9(\pm 16)\%$ lower luminosities, $19(\pm 27)\%$ lower sizes, $40(\pm 23)\%$ lower Sérsic indices. At brighter magnitudes the structural parameters are recovered more accurately. The effects of these biases on our results are discussed in Sect. 4.3.

It is important to note that although the seeing half-radius ($\sim 0''.3$) is similar to the effective radii of the galaxies we are dealing with, we can estimate reasonable structural parameters due to the depth of our images. Our fainter galaxies are 3 magnitudes brighter than the 3σ limit for point sources. This allows us to explore the surface brightness radial profiles to 2.5–3 times the seeing half-light radius.

3.1.2. Comparison between different filters

Mock galaxies are useful to estimate the biases on the recovered structural parameters. However, one can argue that because artificial galaxies are simplistic representations of real galaxies, the errors and bias determinations yield lower limits to the real case. We have checked the internal consistency of our data, comparing the size and shape of our galaxies between the set of near infrared filters used. The seeing and the depth are slightly different amongst the NIR images which allows us to have a robustness test which is not based on simulations. Naturally, this test is only useful under the assumption that the change in the size and the shape of the light profile of the galaxies due to changes in the wavelength along the set of NIR filters is smaller than the intrinsic error in estimating the structural parameters.

Fig. 3 shows the comparison between the sizes and the Sérsic indexes estimated in the K_s band versus the sizes and the Sérsic indexes estimated using J_s ($1 < z < 1.5$) and H ($1.5 < z < 2.6$) bands for galaxies of the MS1054 field with $1 < z < 2.6$. The sizes estimated using the different filters present a $\sim 30\%$ (1σ) of relative scatter between them whereas the scatter for the shapes is larger ($\sim 53\%$).

3.1.3. Size estimates at fixed n

Another possible test to estimate the robustness of our size estimations is to reanalyze the objects using this time the Sérsic index parameter fixed at $n=1$ or $n=4$. We have repeated our analysis for the galaxies in the MS1054 field using the filters which match the V-band rest-frame at every z . All the galaxies are fitted initially with n fixed to 1 and then refitted using n equal to 4. From these two fits we take that with the minimum χ^2 value as representative of the galaxy structural properties.

The comparison between the structural parameters recovered using n fixed and n free is shown in Fig. 4. Galaxies better fitted by an exponential profile ($n=1$) have $0 < n < 2$ when this parameter is left free during the fit. In addition, galaxies

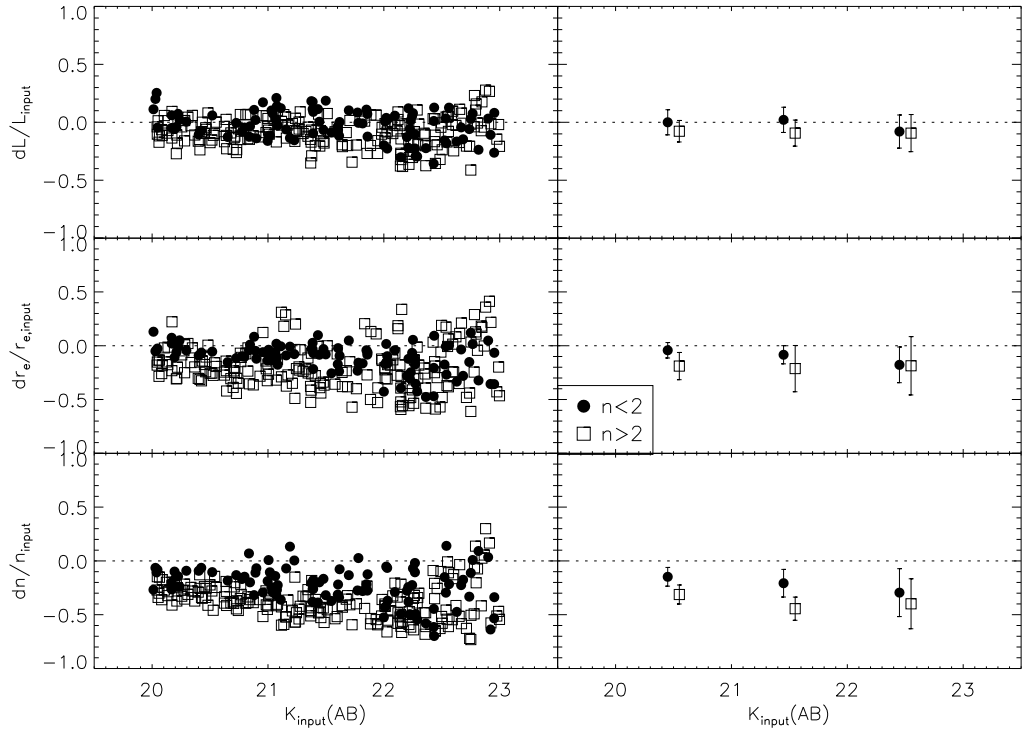


FIG. 1.— The relative error derived from the difference between the input and recovered structural parameters ((output-input)/input) according to our simulations for the FIRES MS1054 field. Solid symbols are used to indicate less concentrated objects ($n < 2$) whereas open symbols imply highly concentrated objects ($n > 2$). The right column of plots shows the mean systematic difference and 1σ error bars.

well fitted by a de Vaucouleurs profile ($n=4$) yield n ranging from 2 to 5. It is interesting to note that there is little overlap between both regimes. From the results presented here, it seems to be possible to discriminate between highly and less concentrated objects using $n=2$ as the separation criterion. In addition, if we assume, as suggested by our simulations, up to a 40% bias on the index n for the high-concentrated objects, an object with original $n=3\text{--}4$ would be identified in our code as $n=1.8\text{--}2.4$. It is important to note that our criterion for separating the galaxies using $n=2$ would be similar to using $n=2.5$ in a case where the index n was less biased than in the current analysis. In what follows, we will take advantage of this to facilitate a comparison of our results with those found at lower z (see Sections 4 and 5.1)

The sizes estimated using n fixed or n free during the fit show very good agreement with only $\sim 21\%$ (1σ) of relative scatter between them. The sizes estimated using n fixed are, on average, $\sim 4.5\%$ larger.

3.1.4. Comparison with NICMOS data

We have recently obtained deep H-band NICMOS images of the HDF-S. These NICMOS data consist of 8 pointings of camera 3 (52" x 52", 0.203"/pix). Each pointing is the combination of 6 sub-pixel dithered exposures, with a total exposure time of 1.5 hours. The final mosaic was assembled using the *drizzle* task and has a pixel scale of 0.119" to match our ISAAC ground-based data¹³. A detailed presentation of this

dataset and an analysis of the sizes of the galaxies in this image will be presented in Zirm et al. (2005).

We have 25 galaxies in common between ISAAC and NICMOS images in the redshift range $1.5 < z < 2.6$ for which we analyze the H-band images. We found a good correlation between the sizes measured in the NICMOS images compared with those measured with ISAAC. The scatter is 33% (1σ) with a slight bias suggesting that the sizes estimated from the ISAAC images could be overestimated by about 7%.

For consistency with the rest of our data (which are retrieved from ISAAC images) we present our results without attempt to correct for the above bias. However, in Fig. 12 we show what would be the effect on our relations if our sizes were biased by a 7% error. The main conclusions of our paper are unaffected.

3.2. Selection Effects

In practice, any image presents a surface brightness limit beyond which the sample is incomplete. To characterize this limit is particularly important for high- z samples where the effects of the cosmological surface brightness dimming are severe. For a given total flux limit, the surface brightness limit translates into an upper limit on the size for which a galaxy can be detected.

To determine the completeness of the FIRES MS1054 K_s -band image we have created a set of 10^5 mock sources with intrinsic exponential profiles, K_s -band total magnitudes between 18 and 24 mag, effective radius r_e between 0.03 and 3 arcsec and inclination angles between 0 and 90 degrees. These sources are placed randomly on the real image 20 at a

¹³ The ISAAC pixel scale is actually 0.147"; however, we resampled the ISAAC pixels to 3×3 blocked HDF-S WFPC2 pixels.

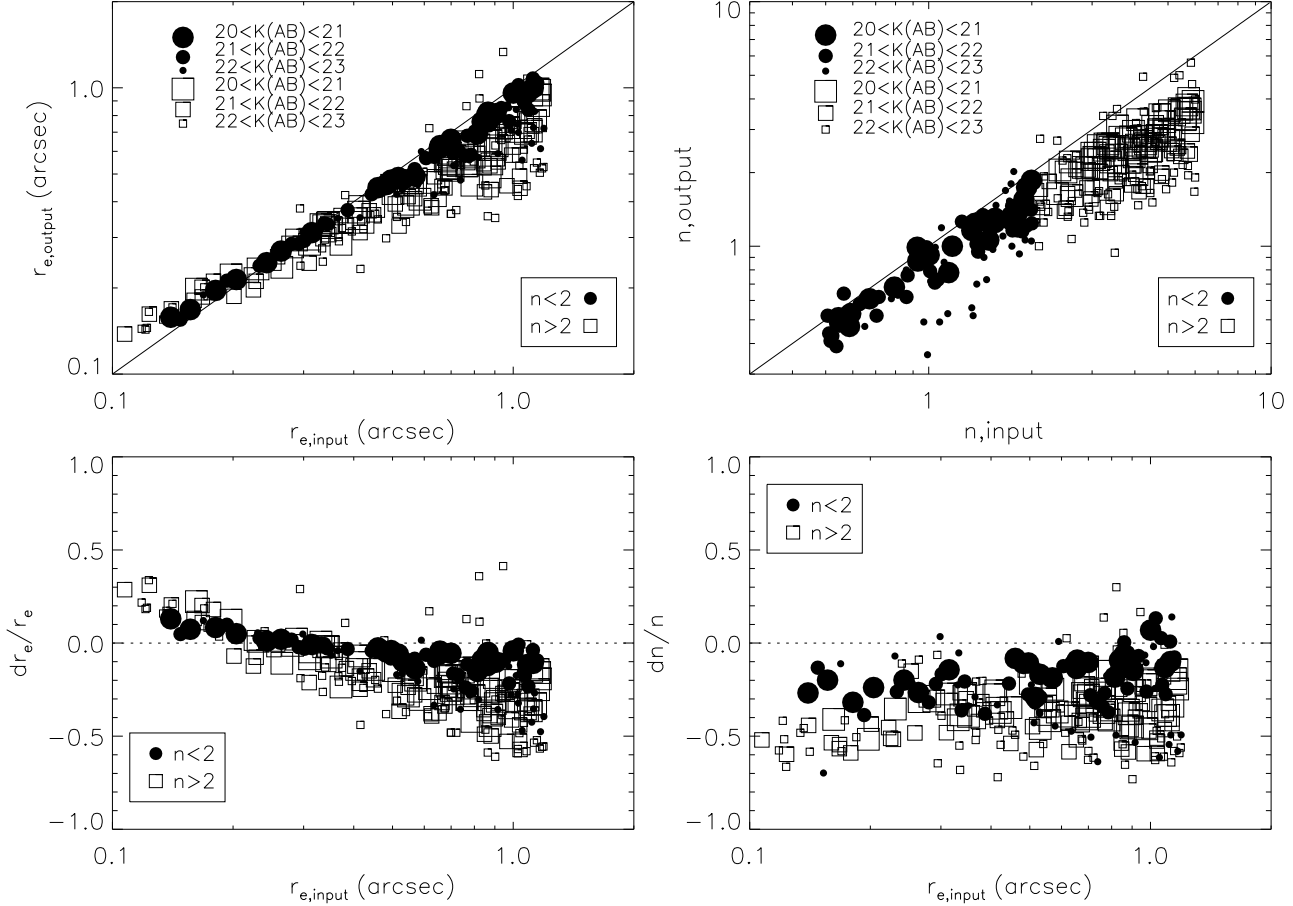


FIG. 2.— Galaxy size-measurement bias: The figure shows a comparison between input and recovered structural parameter values in our simulations for the FIRES observations of the MS1054 field. *Top Left*: The relation between measured and the input intrinsic half-light radius (before seeing convolution). *Top Right*: The relation between measured and input seeing deconvolved Sérsic index n . *Bottom Left*: The relative error between the input and the measured seeing deconvolved effective radius ($dr_e/r_e = (r_{e,\text{output}} - r_{e,\text{input}})/r_{e,\text{input}}$) versus the input effective radius. *Bottom Right*: The relative error between the input and the measured seeing deconvolved Sérsic index n ($dn/n = (n_{\text{output}} - n_{\text{input}})/n_{\text{input}}$) versus the input effective radius. Solid symbols are used to indicate less concentrated objects ($n < 2$) whereas open symbols imply highly concentrated objects ($n > 2$).

time and extracted as for the real source detection. On doing that we construct a completeness map giving the number of recovered sources over number of artificial sources per input magnitude bin and input $\log(r_e)$ bin (see Fig. 5). A equivalent analysis for the HDF-S field is presented in Fig. 8 of Trujillo et al. (2004). Readers more interested in the completeness simulations are referred to Förster Schreiber et al. (2005). It is important to note that in selecting exponential profiles ($n=1$) for estimating our completeness map we are being conservative from a detection standpoint. Galaxies with larger n , and consequently more centrally concentrated, would be much easier to detect at a given magnitude.

As a second step to analyze the effect of completeness in our sample we have probed whether the size distribution of our objects could be affected by the completeness. In Fig. 5 we show the completeness for three different magnitude intervals: $21.5 < K_s < 22$, $22 < K_s < 22.5$ and $22.5 < K_s < 23$ as a function of the size. In addition, we overplot the size distribution (arbitrarily normalized to have a value of 1 at the peak) of real galaxies in the same intervals. This comparison shows that real galaxy distributions start decreasing at much smaller sizes than the simulations. This indicates that our sample is not affected by incompleteness at larger sizes.

Interestingly, Bouwens et al. (2004) show, using UDF images, that the principal effect of increased depth is to add

galaxies at fainter magnitudes, not larger sizes, demonstrating that high- z galaxies are predominantly compact and that large low surface brightness objects are rare. This result provides independent corroboration of our analysis.

We have also quantified the mass and luminosity limits implied by our observed magnitude limit. In doing so we try to serve the dual purpose of maximizing the number of objects in our sample while simultaneously reducing systematic biases on the final results. We determine our rest-frame luminosity limit using the K_s magnitude and the expected color of an Scd template at $z = 2.5$, the center of our highest redshift bin. For $K_s = 23.5$ this limit is $L_V > 3.4 \times 10^{10} h_{70}^{-2} L_\odot$. Above this limit we are complete at all redshifts $z \lesssim 2.5$ in the HDF-S field. We adopt the same limit for the MS1054 data acknowledging that we will be missing galaxies in our higher redshift bin with $23 < K_s < 23.5$. As shown in Figs. 7 and 9, however, the distributions in size, luminosity, and mass of objects in the MS1054 and the HDF-S fields are similar and we make the assumption that this incompleteness in the highest redshift MS1054 data will not significantly bias our results.

We choose two separate means of defining a limit in mass. For our first mass limit we choose the lowest observed mass in our combined sample at $z \sim 2.5$ (see Fig. 6). This limit is $M_* > 3 \times 10^{10} h_{70}^{-2} M_\odot$. We realize that only the objects with the lowest mass-to-light ratios will be detectable at these

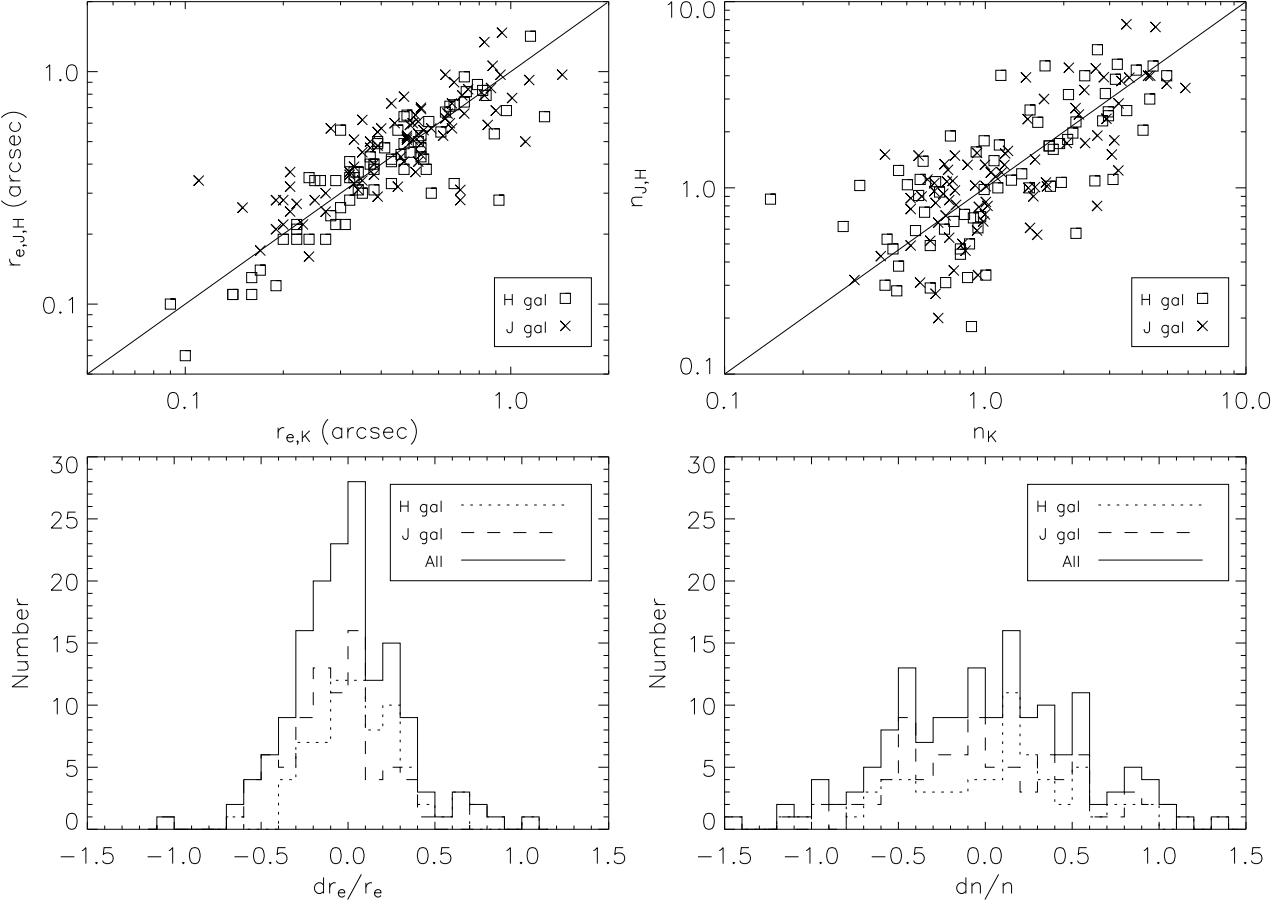


FIG. 3.— *Upper panels:* Comparison between the profile shapes and size estimates using the FIRES J_s or H filters versus the K_s band for all the galaxies in the MS1054 field with $1 < z < 2.6$. To match the rest-frame optical V-band, galaxies with $1 < z < 1.5$ were observed in the J_s -band, and galaxies with $1.5 < z < 2.6$ were observed in the H -band. *Lower panels:* The relative difference between the size and the shape parameter measured in the different filters: $dr_e/r_e = 2 \times (r_{e,K} - r_{e,J,H})/(r_{e,K} + r_{e,J,H})$ and $dn/n = 2 \times (n_K - n_{J,H})/(n_K + n_{J,H})$. The standard deviation for the sizes is $\sim 30\%$ and for the shapes $\sim 53\%$.

masses and that we are incomplete to objects of higher mass-to-light ratios. Nonetheless we use this limit to maximize the total number of objects in our sample, keeping in mind that we may experience systematic biases from our mass incompleteness. As a more conservative approach we also choose a mass limit corresponding to the maximum stellar mass-to-light ratio expected at $z \sim 2.5$. We use a maximally old single stellar population from Bruzual & Charlot (2003) with solar metalicity and a Salpeter (1955) IMF. At $z \sim 2.5$ the Universe is ~ 2.6 Gyr old for our cosmology and the resultant mass-to-light ratio is 1.93. Coupled with our luminosity limit of $3.4 \times 10^{10} h_{70}^{-2} L_\odot$, this yields a mass limit of $M_* > 6.6 \times 10^{10} h_{70}^{-2} M_\odot$. Above this limit we are complete to objects of every stellar mass-to-light ratio, although we have very few objects and our random errors will be large. The differences between results using these two limits are discussed in the end of § 6. As done for the luminosity threshold we adopt the limits for the HDF-S for the whole sample.

4. THE OBSERVED LUMINOSITY/STELLAR MASS VS SIZE RELATIONS AT HIGH-Z

4.1. *Luminosity vs size*

We now present the relation between luminosity and the rest-frame V-band size, covering the redshift range $1 < z < 3.2$ for the HDF-S and the MS1054 fields. This redshift regime is selected to avoid the influence of cluster galaxies at $z=0.83$ in

the MS1054 field and to maintain our analysis of the high- z galaxies in the optical rest-frame. We convert our measured angular sizes to physical sizes using the photometric redshift (or the spectroscopic value when available) determined for each object.

In Fig. 7 our sample is split in three different redshift bins: $1 < z < 1.4$, $1.4 < z < 2$ and $2 < z < 3.2$. This separation allows us to study the galaxies in roughly equal time intervals of ~ 1.2 Gyr.

The top row shows the luminosity-size relation for the full sample. The middle row and the bottom row show the same relation but this time separating the galaxies by their concentration.

Overplotted on our observed distributions are the mean and dispersion of the distribution of the Sérsic half-light radii from the Sloan Digital Sky Survey (SDSS; York et al. 2000) galaxies. We use the “local” SDSS sample for reference. The sizes are determined from a Sérsic model fit (Blanton et al. 2003). The characteristics of the sample used here are detailed in Shen et al. (2003). The mean of the SDSS galaxies redshift distribution used for comparison is 0.1. We use the sizes and the shapes estimated in the observed r-band as this closely matches the V-band restframe filter at $z \sim 0.1$. The luminosity of the SDSS galaxies in the restframe V-band are estimated by interpolating between the restframe g-band and r-band luminosities (S. Shen, private communication).

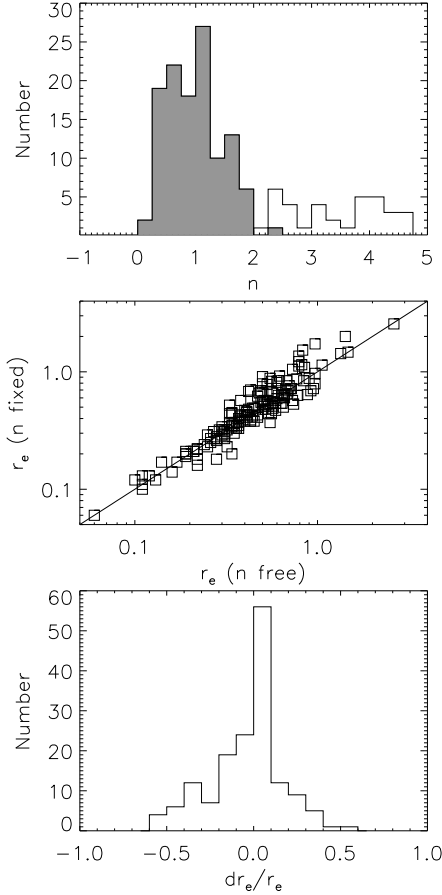


FIG. 4.— *Top Panel.* The grey histogram shows the Sérsic index distribution (when leaving this parameter free in the fitting process) for the subset of galaxies which are better fit with a fixed Sérsic parameter to $n=1$ whereas the open histogram shows the shape distribution for the galaxies well fitted with $n=4$. *Center Panel.* The comparison between the size estimated using n free versus the size estimated using n fixed to 1 or 4. *Bottom Panel.* The relative difference between the size estimated using n fixed or free: $dr_e/r_e=2\times(r_{e,nfree}-r_{e,nfixed})/(r_{e,nfree}+r_{e,nfixed})$. The scatter between both sizes estimates is $\sim 21\%$ (1σ), with little ($\sim 4.5\%$) mean offset. The structural parameters are estimated using the filters which match the V-band restframe at every z .

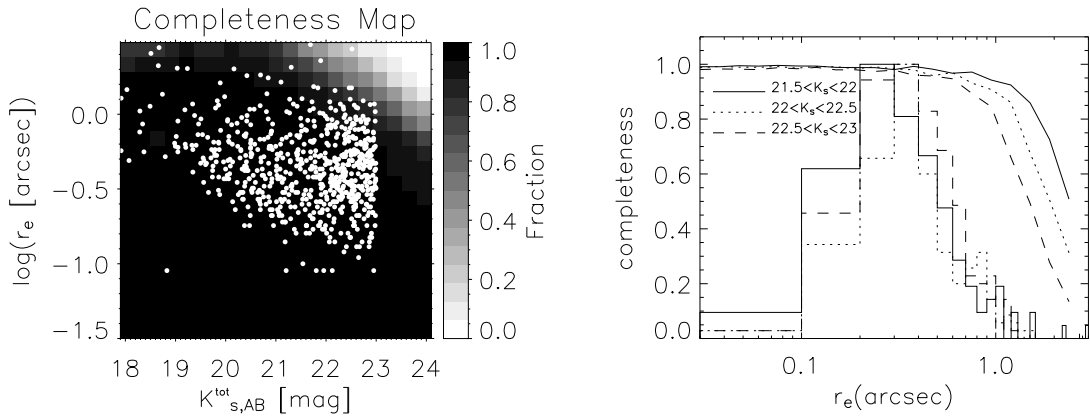


FIG. 5.— *Left Panel.* Completeness map for exponential objects placed on our K_s band image of the MS1054 field. The grey-scale map reflects the ratio between input and recovered objects per input magnitude and $\log(r_e)$ bin. Overplotted on the map is the distribution of the full sample of K_s band selected objects in the MS1054 field. *Right Panel.* The completeness for three different magnitude intervals: $21.5 < K_s < 22$, $22 < K_s < 22.5$ and $22.5 < K_s < 23$ as a function of the size (smooth curves). Overplotted are the size distributions (arbitrarily normalized to have a value of 1 in the peak) of real galaxies in the same intervals (histograms). The observed size distribution starts decreasing at much smaller sizes than the completeness limit and does not show the same dependence on magnitude. This indicates that our sample is not significantly affected by incompleteness of the largest galaxies at a given magnitude.

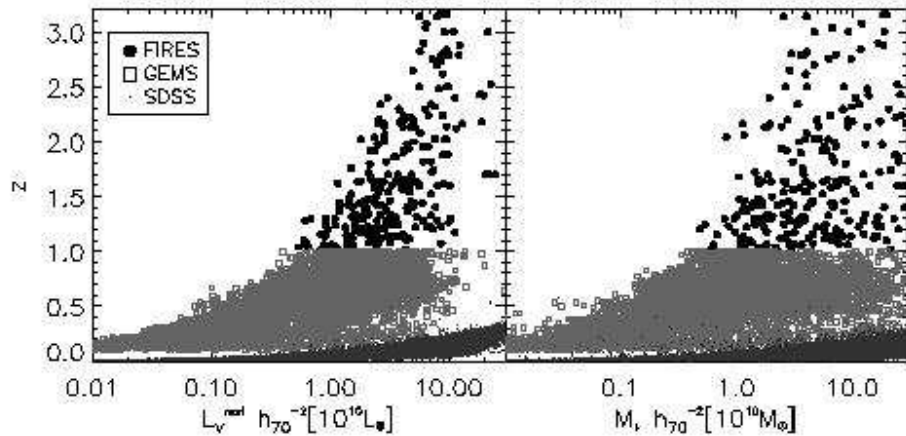


FIG. 6.— The L_v – z and M_* – z diagrams for the combined data set used in the present analysis. Solid points correspond to the FIREs galaxies in the HDF–S and the MS1054 fields, open squares are GEMS galaxies (McIntosh et al. 2005; Barden et al. 2005) and dots are the SDSS galaxies (Shen et al. 2003). Only the most luminous and the most massive objects can be homogeneously explored along the full redshift range. Since the mean redshift is our highest redshift bin is ~ 2.5 , only galaxies with $L_v \gtrsim 3.4 \times 10^{10} h_{70}^{-2} L_\odot$ can be studied as a homogeneous sample. Objects with the lowest mass–to–light ratios can be homogeneously explored if their masses are $M_* \gtrsim 3 \times 10^{10} h_{70}^{-2} M_\odot$. We are complete to objects of every stellar mass–to–light ratio if $M_* \gtrsim 6.6 \times 10^{10} h_{70}^{-2} M_\odot$ (see text for details).

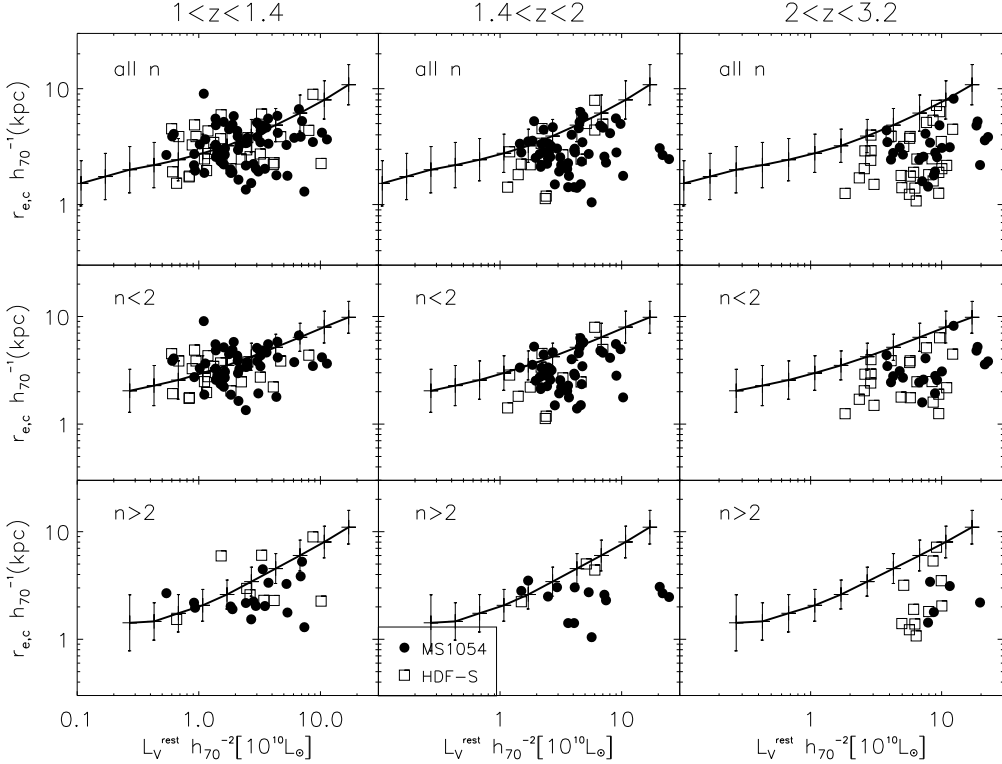


FIG. 7.— Distribution of the rest-frame optical sizes vs. the rest-frame V-band luminosities for all galaxies from FIRES. Galaxies from the HDF-S field (Labbé et al. 2003) are shown by open squares and galaxies from the MS1054 field (Förster Schreiber et al. 2005) by filled circles. The different rows show the galaxies separated according to their Sérsic index concentration parameter. Overplotted on the observed distribution of points are the mean and dispersion of the distribution of the Sérsic half-light radius of the SDSS galaxies (in the “V-band”) as a function of the V-band luminosity. The second and third row show the SDSS distributions separating into late and early type respectively. For clarity individual error bars for the FIRES data are not shown; the mean size relative error is 30%.

In the first row, our sample is compared to the total population observed by SDSS, whereas in the second row we compare with the galaxies classified by Shen et al. as late-type and in the third row with those classified as early-type. Their early or late-type classification is based on the Sérsic index: galaxies with $n < 2.5$ are considered late-types and galaxies with $n > 2.5$ are identified as early-types. It is important to note that using $n=2$ as the criterion for the separation between early- and late-type galaxies in the SDSS does not produce a significant change in the luminosity- and stellar mass-size relations (S. Shen, private communication). This is as expected because of the scatter between the Sérsic index n and the Hubble Type relation (see e.g. Fig. 1 of Ravindranath et al. 2004). Consequently, changing from $n=2$ to $n=2.5$ (or vice versa) does not change substantially the morphological type of the galaxies under study, and therefore, the effect on the luminosity-size or stellar mass-size relations is small.

Returning now to the redshift evolution, Fig. 7 shows that at a given luminosity, galaxies are progressively smaller at higher z . Of course, this evolution of the luminosity-size relation can be interpreted differently: at a given size, galaxies were more luminous at higher z .

To quantify the evolution of these relations as a function of redshift, we show in Fig. 8 the ratio between the observed size and the expected size (at a given luminosity) from the SDSS distribution versus z . To estimate the expected size from SDSS at a given luminosity we interpolate linearly between

the SDSS points when necessary. From this plot the evolution in size (at a given luminosity) with z is evident. Galaxies with $L_v \gtrsim 3.4 \times 10^{10} h_{70}^{-2} L_\odot$ at $z \sim 2.5$ are ~ 2.5 times smaller than for equally luminous galaxies today. In the second row of this figure we show the evolution of the mean and the dispersion (large error bars) of the above ratio. These quantities are estimated in the same redshift bins as stated above. The small error bars enclose the 2σ uncertainty of the means. To evaluate these error bars we have used a bootstrapping method.

4.2. Stellar mass vs size

We have also explored the relation between stellar mass and size for our sample (Fig. 9). The stellar mass-size distribution evolves less than the luminosity-size relation at high- z . The stellar mass-size relation presents more scatter than the luminosity-size relation because the stellar mass is an indirectly inferred property. Galaxies with $M_* \gtrsim 3 \times 10^{10} h_{70}^{-2} M_\odot$ and $z > 1.5$ have slightly smaller sizes than do equally massive galaxies today. This is illustrated in Fig. 10 where we show the ratio between the observed size and the expected size (at a given stellar mass) according to the SDSS local sample.

The SDSS stellar masses used in Shen et al. (2003) are derived from stellar absorption line indices centered on the inner region of the galaxies whereas the present work uses colors integrated over the full galaxy. As discussed in Kauffmann et al. (2003) this difference in techniques is particularly important for brighter galaxies as they have strong color gradients, such that the central colors are not indicative of the

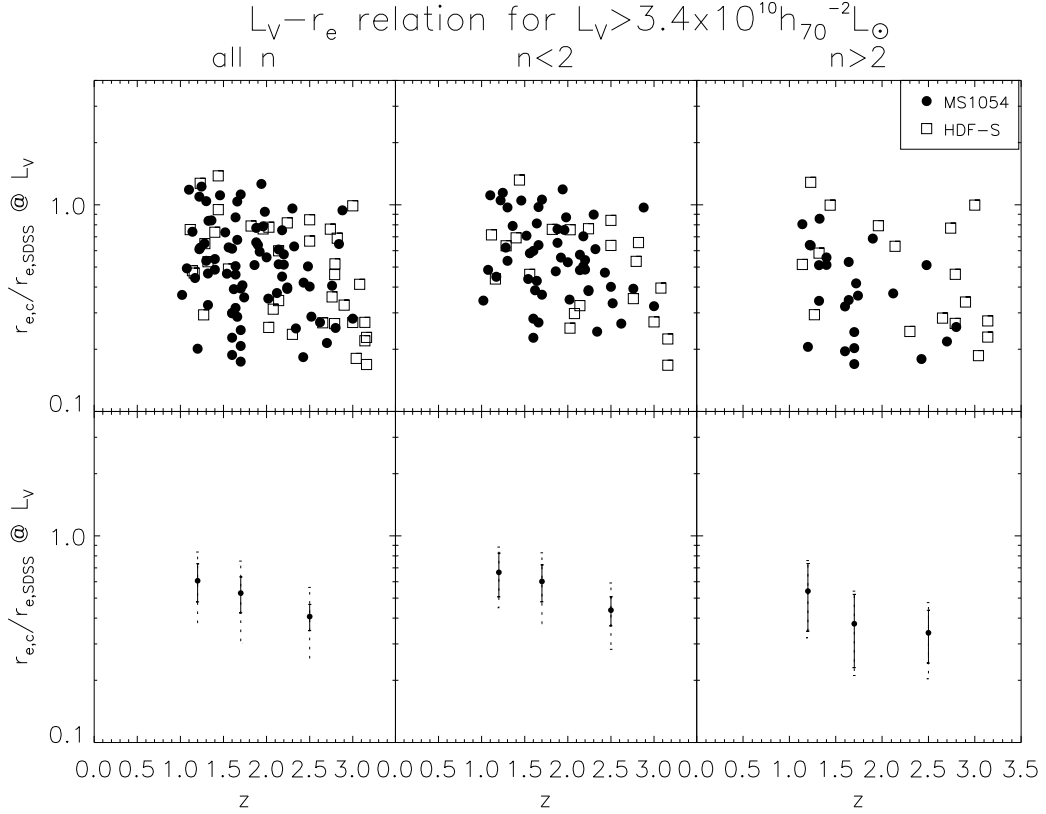


FIG. 8.— Redshift evolution of the size–luminosity relation for FIREs galaxies: the figure shows the ratio between the observed size (at a given luminosity) and the mean size of equally luminous present-day galaxies from the local SDSS sample as a function of z . The upper panels show the individual objects whereas the lower panels show the dispersion (dotted error bars) of the distribution and the uncertainty (2σ) at the mean determination (solid error bars). The figure shows that galaxies of a given luminosity were physically smaller at early epochs (or higher redshift). Alternatively, the plot shows that galaxies of a given size were more luminous at higher z .

luminosity weighted total colors. According to that work the mass–to–light ratio derived from line indices are biased to higher values than those measured from integrated colors. To avoid this problem, we have re–estimated the stellar masses of SDSS for this work using the restframe ($g–r$) color (S. Shen, private communication) and applying the transformation suggested for this color in Bell et al. (2003). This transformation is based on a Kroupa (2001) IMF. To match their values with the FIREs data (which uses a Salpeter IMF) we apply the transformation suggested in Kauffmann et al. (2003): $M_{IMF,Salpeter} = 2 \times M_{IMF,Kroupa}$.

4.3. Robustness of the Luminosity–size and stellar mass–size estimates

The luminosity– and mass–size relations presented in the previous sections are based on our direct measurements without making any attempt to correct for possible biases in the structural parameters as indicated by the simulations. To check whether the presented results are robust we have repeated our analysis correcting this time the observed structural parameters following the indications of our simulations. In addition, we have also repeated our analysis using the size estimation from the fits using n fixed. We summarize the results of these tests on Fig. 11.

As expected, due to the smaller sub–sample of galaxies and the larger corrections suggested by the simulations, the least robust results are for galaxies with the larger light concentration ($n > 2$). However, it is interesting to note that all the

estimates of the mean relation are in agreement within $\sim 1\sigma$. As most of our galaxies have $n < 2$, the corrections are small for most of the sample. Consequently, the relations using the corrections suggested by the simulations do not change our main results. In addition, when we compare our relations using n free with those obtained using n fixed to $n=1$ or $n=4$, we do not observe systematic effects.

We have also studied whether the weak magnification lensing of the MS1054–03 foreground cluster can affect the result of our analysis. The cluster mass distribution has been modeled by Hoekstra, Franx & Kuijen (2000). The average background magnification effects over the field of view covered by FIREs observation range from a few % to 25% between $z=1$ to 4. The magnification is most significant in the immediate vicinity of the cluster central region. The Einstein radius r_E of this cluster is estimated to be ~ 15 arcsec. We have removed from our sample all the galaxies located within $2r_E$ (this implies 9 objects). Outside this region the magnification is expected to be very small. The result of removing these galaxies in our relations is shown in Fig. 11. As expected from the small number of objects within $2r_E$ the effect on our relations is very tiny.

The above tests indicate that the results presented in this paper are robust. Because the main results of this paper are insensitive to the corrections, we perform our analysis based purely on the direct measurements. Applying these corrections artificially increases the scatter of our relations because of the necessary approximations when correcting. We find

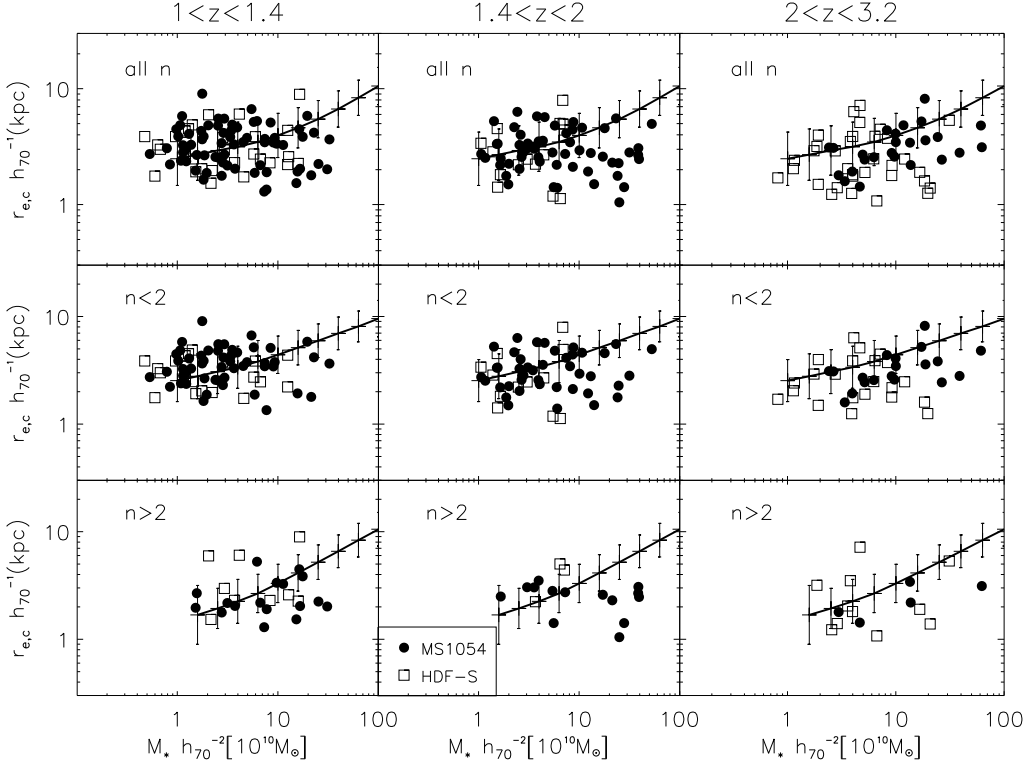


FIG. 9.— Distribution of rest-frame optical sizes vs. the stellar masses for FIRE galaxies. Analogously to Fig. 7 galaxies from the HDF-S field are shown by open squares and galaxies from the MS1054 field by filled circles. The different rows show the galaxies separated according to their Sérsic index shape parameter. Overplotted on the observed distribution of points are the mean and dispersion of the distribution of the Sérsic half-light radius of the SDSS galaxies as a function of the stellar mass. The second and third row show the SDSS distributions separated into late and early type respectively. For clarity, individual error bars are not shown. The mean size relative error is 30%.

that the increase of the scatter is $\sim 20\text{--}40\%$ in the corrected distributions related to those based on the direct estimations.

5. ANALYSIS

5.1. Comparison of FIRE data to the evolution at $z < 1$

Several analyses of the luminosity-size evolution of galaxies in the optical rest-frame up to $z \sim 1$ have been carried out (Im et al. 1996; 2002, Lilly et al. 1998, Schade et al. 1999, Simard et al. 1999, Ravidranath et al. 2004; Trujillo & Aguerri 2004; McIntosh et al. 2005; Barden et al. 2005). These studies seem to agree on a moderate decrease of the surface brightness of the galaxies towards the present: < 1 mag in the V-band restframe (or equivalently a decrease in size at a given luminosity of $\lesssim 35\%$).

In order to make a consistent comparison at lower redshifts with FIRE, we use the data from the largest sample currently available at intermediate redshift: the GEMS survey (Rix et al. 2004). GEMS is a large-area (800 arcmin 2) two-color (F606W and F850LP) imaging survey with the ACS on the HST to a depth of $m_{AB}(\text{F606W}) = 28.3(5\sigma)$ and $m_{AB}(\text{F850LP}) = 27.1(5\sigma)$ for compact sources. Focusing on the redshift range $0.2 \leq z \leq 1$, GEMS provides morphologies and structural parameters for nearly 10,000 galaxies for which redshift estimates, luminosities, and SEDs exist from COMBO-17 (Classifying Objects by Medium-Band Observations in 17 Filters; Wolf et al 2001, 2003).

The luminosity-size and stellar mass-size relations of this survey are presented in Barden et al. (2005; late-type galax-

ies) and McIntosh et al. (2005; early-type galaxies). The GEMS late- and early-type separation criteria is based on the Sérsic index n . Late-types are defined through $n < 2.5$, and early-types through $n > 2.5$ and a color within the “red-sequence” (Bell et al. 2004). We have checked that adopting $n=2$ instead of $n=2.5$ as the separation criterion does not produce a significant change in their results. The stellar masses of the GEMS survey used in the present work are derived in the same way as those in FIRE¹⁴. Using their measurements of size, luminosity, mass, redshift and completeness we have repeated the same analysis as for the FIRE sample. To assure homogeneity with the FIRE sample we have only selected GEMS galaxies with $L_V > 3.4 \times 10^{10} h_{70}^{-2} L_\odot$ (in the case of the luminosity-size relation) and $M_* \gtrsim 3 \times 10^{10} h_{70}^{-2} M_\odot$ (in the case of the stellar mass-size relation). The resulting size evolution from both surveys together are shown in Fig. 12 and Table 2.

From this comparison we see that the $z < 1$ evolution (GEMS) and $z > 1$ evolution (FIRE) derived from two independent analyses and data sets match very well. We discuss this in more detail in Sect. 6.

5.2. Comparison of FIRE to other works at $z > 1$

Recently, Papovich et al. (2005) have measured the evolution of the sizes in the B-band restframe for galaxies in

¹⁴ In Barden et al. (2005) and McIntosh et al. (2005) the GEMS stellar masses are also estimated from stellar populations models, finding no differences in the resulting stellar mass-size relation.

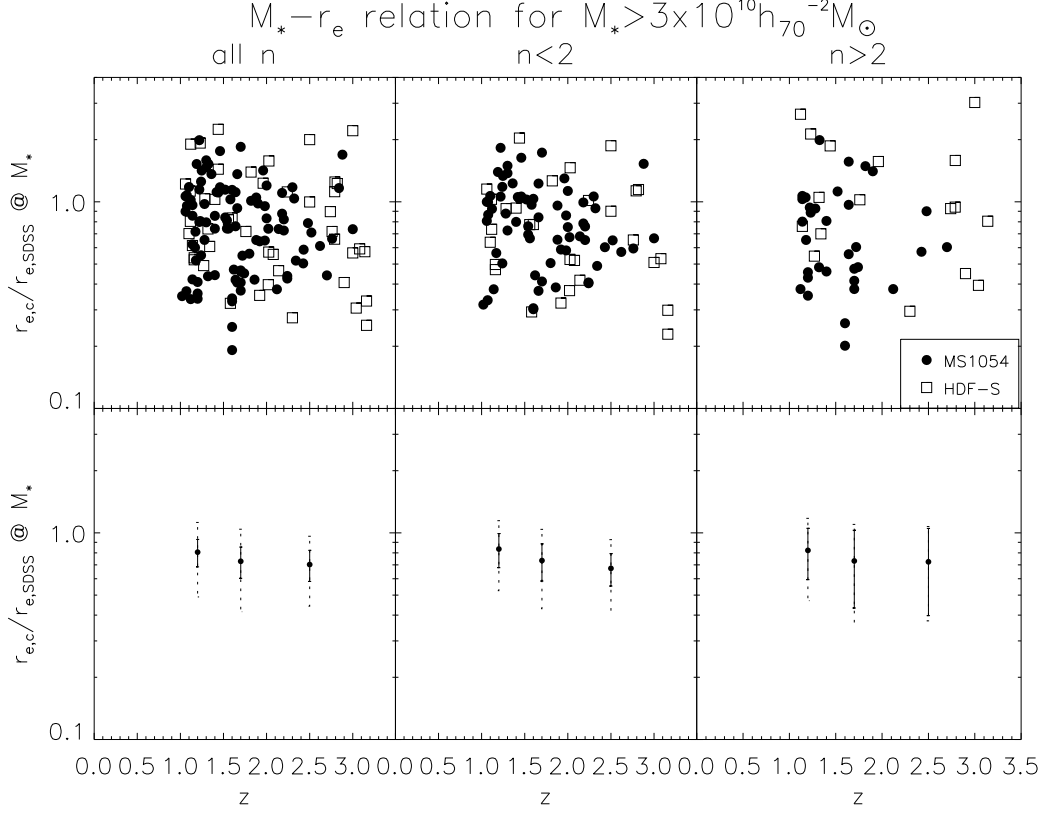


FIG. 10.— The ratio between observed size of FIRES galaxies and the size (at a given stellar mass) expected from the local SDSS sample shown as a function of z . The upper panels show the individual objects whereas the lower panels show the dispersion (dotted error bars) of the distribution and the uncertainty (2σ) at the mean determination (solid error bars). The size at a given mass evolves moderately with z .

TABLE 2
MEAN SIZE EVOLUTION VS REDSHIFT

$\langle z \rangle$	$n < 2$	$n > 2$
$L_V \gtrsim 3.4 \times 10^{10} h_{70}^{-2} L_\odot$		
0.1	1	1
0.3	0.88 ± 0.13	0.85 ± 0.15
0.5	0.80 ± 0.16	0.70 ± 0.15
0.65	0.79 ± 0.07	0.68 ± 0.06
0.9	0.76 ± 0.06	0.58 ± 0.08
1.2	0.67 ± 0.16	0.54 ± 0.19
1.7	0.60 ± 0.12	0.38 ± 0.15
2.5	0.44 ± 0.07	0.34 ± 0.10
$M_* \gtrsim 3 \times 10^{10} h_{70}^{-2} M_\odot$		
0.1	1	1
0.3	0.88 ± 0.14	0.92 ± 0.11
0.5	0.84 ± 0.09	0.76 ± 0.08
0.65	0.90 ± 0.05	0.86 ± 0.06
0.9	0.90 ± 0.07	0.84 ± 0.10
1.2	0.84 ± 0.15	0.82 ± 0.23
1.7	0.73 ± 0.15	0.73 ± 0.30
2.5	0.67 ± 0.12	0.72 ± 0.32

NOTE. — Col. (1): Mean redshift of the bin
Col. (2) and Col. (3) $r_e(z)/r_e(0.1)$ and the 2σ uncertainty on the mean values

the HDF-N using WFPC2 and NICMOS imaging. At $z \sim 2.3$ they find a mean value of 2.3 ± 0.3 kpc for $M(B) \leq -20.0$. For galaxies with $M(V) \leq -21.5$ at $z \sim 2.5$ we have 2.8 ± 0.3 kpc. In both cases the error represents the uncertainty on the mean.

The difference between the values can be understood because our magnitude limit selects a population of galaxies approximately 1 mag brighter in the B-band restframe at that redshift ($(B-V)_{rest} \sim 0.4$ at $z \sim 2$; Rudnick et al. 2003) than the Papovich et al. work. At lower redshift we can make a more consistent comparison because our sample is complete at fainter magnitudes. On doing that, we find at $z \sim 1.2$: 3.4 ± 0.3 kpc for $M(V) \leq -21.5$ or 3.2 ± 0.2 kpc for $M(V) \leq -20.5$. Assuming $(B-V)_{rest} \sim 0.55$ at $z \sim 1$ (Rudnick et al. 2003) this last value can be compared with the value found in Papovich et al. at $z \sim 1$: 3.2 ± 0.3 kpc for $M(B) \leq -20.0$. The agreement is encouraging taking into account the different image quality and methods used for retrieving the half-light radii.

At even larger redshifts, analysis of $1 < z < 6$ galaxies based on the optical bands (and consequently, matching the UV rest-frame) show a strong decrease in size at a given UV luminosity. This decrease scales with z as: $(1+z)^{-1.5}$ (Ferguson et al. 2004) or as $(1+z)^{-1}$ (Bouwens et al. 2004). In agreement with these results, in the redshift range $1 < z < 3$ the sizes at a given V-band luminosity presented here are well described by $(1+z)^{-0.9 \pm 0.2}$. Consequently, the shape of the evolution is similar in the UV and in the V-band restframe at least in the above redshift range.

5.3. Analytical description of the size evolution

To provide with an analytical description of the rest-frame size evolution of the galaxies in the redshift range $0 < z < 3$, we have fitted the observed size evolution at a given luminosity ($L_V \gtrsim 3.4 \times 10^{10} h_{70}^{-2} L_\odot$) and at a given stellar mass ($M_* \gtrsim 3 \times 10^{10} h_{70}^{-2} M_\odot$) to two different analytical functions:

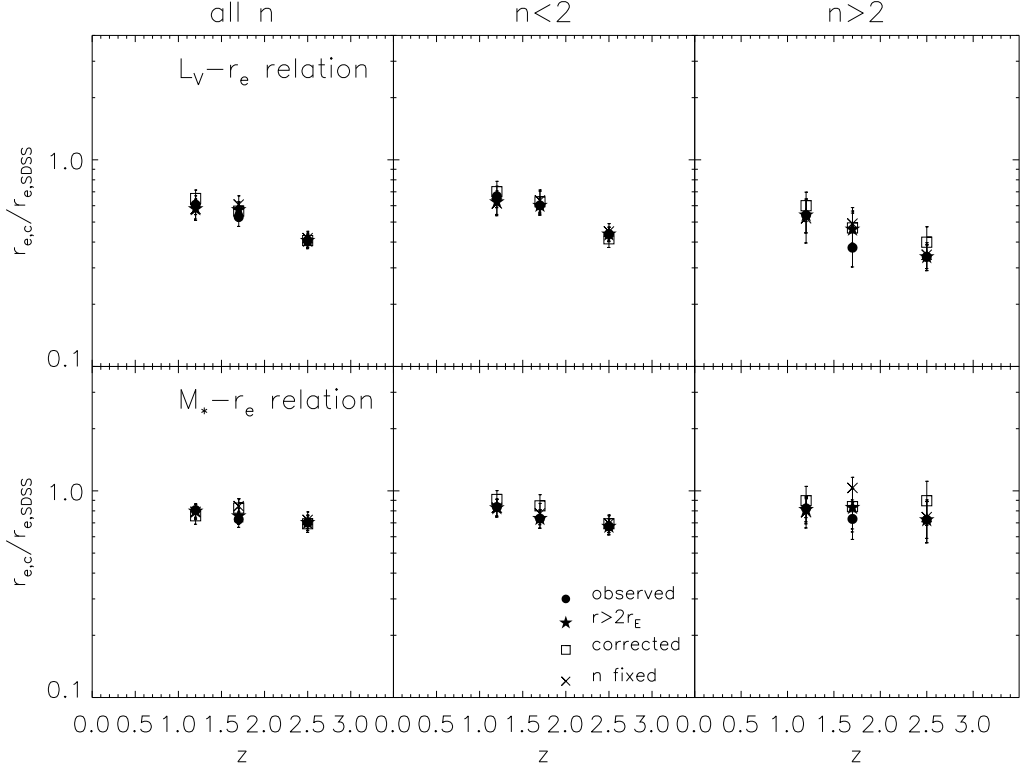


FIG. 11.— Comparison between three different estimates of the mean luminosity- and stellar mass-size distributions: the direct estimates (solid points), the estimates omitting the galaxies inside two Einstein radii ($r_E \sim 15''$; Hoekstra et al. 2000) of the MS1054 cluster (solid stars), the estimation using the corrections suggested from our simulations (open squares) and the estimation using fits where the Sérsic index n is fixed to 1 or 4 (crosses). The error bars show the 1σ uncertainty in estimating the mean of the distributions. All the points are in agreement within $\sim 1\sigma$. For clarity, bars showing the intrinsic dispersion of the relations are not included.

TABLE 3
ANALYTICAL FITS TO THE SIZE EVOLUTION

Fit	α	$\tilde{\chi}^2$
$L_V \gtrsim 3.4 \times 10^{10} h_{70}^{-2} L_\odot$ ($n < 2$)		
$(1+z)^\alpha$	-0.65 ± 0.05	0.41
$H^\alpha(z)$	-0.65 ± 0.05	0.15
$L_V \gtrsim 3.4 \times 10^{10} h_{70}^{-2} L_\odot$ ($n > 2$)		
$(1+z)^\alpha$	-0.97 ± 0.07	0.15
$H^\alpha(z)$	-0.98 ± 0.07	0.97
$M_* \gtrsim 3 \times 10^{10} h_{70}^{-2} M_\odot$ ($n < 2$)		
$(1+z)^\alpha$	-0.30 ± 0.07	0.28
$H^\alpha(z)$	-0.32 ± 0.07	0.28
$M_* \gtrsim 3 \times 10^{10} h_{70}^{-2} M_\odot$ ($n > 2$)		
$(1+z)^\alpha$	-0.41 ± 0.10	0.58
$H^\alpha(z)$	-0.47 ± 0.12	0.81

NOTE. — Col. (1): Analytical expression used to fit the data Col. (2) Value of the parameter measured including 1σ error bar and Col. (3) Reduced $\tilde{\chi}^2$ value of the fit.

a) $(1+z)^\alpha$ and b) $H^\alpha(z)$. To avoid confusion with lines drawn from comparison with theoretical models we do not overplot these fits in Fig. 12. The results of our fits, however, are shown in Table 3.

6. DISCUSSION

We have greatly expanded the FIRE sample of galaxy rest-frame optical size measurements, compared to Trujillo et al. (2004), and have combined these with data from GEMS and SDSS. This combined data set allows us to analyze the evolution of the luminosity-size and the stellar mass-size relations for luminous ($L_V \gtrsim 3.4 \times 10^{10} h_{70}^{-2} L_\odot$) and massive ($M_* \gtrsim 3 \times 10^{10} h_{70}^{-2} M_\odot$) galaxies over 80% of the Universe's age ($0 < z < 3$). During that time their luminosity-size relation has changed strongly but the stellar mass-size relation has evolved significantly less than the luminosity-size relation. As suggested in Trujillo et al. (2004) these two results can be reconciled when we take into account the strong mass-to-light ratio evolution that galaxies have experienced in the past. Such M/L evolution must also play a big role in explaining the strong $L_{UV} - r_{e,UV}$ evolution seen in high- z samples (e.g. Ferguson et al. 2003).

Beyond the empirical result, it is of interest to compare the observed evolution with the theoretical predictions. In Fig. 12 we show the expectations from semianalytical hierarchical and infall models for disk-like galaxies compared to the observed size evolution. We first concentrate our attention on the evolution of the sizes at a given luminosity. The semianalytic hierarchical Mo et al. (1998) model makes predictions on the disk size evolution at a given halo mass or circular velocity, assuming that the disk mass is a fixed fraction of the halo mass. If one then identifies Mo et al. disk mass with the stellar mass, or even the stellar luminosity (as done e.g. by Ferguson et al. 2003) then a size-luminosity scaling of

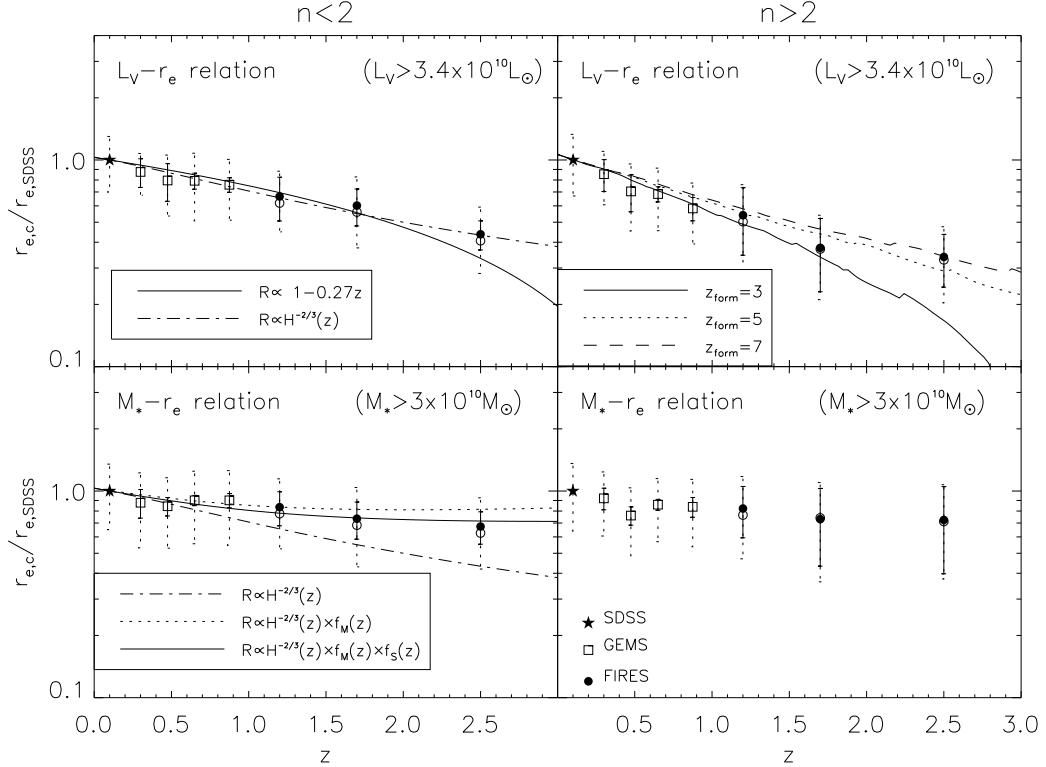


FIG. 12.— Redshift evolution of the ratio between the observed size and the present-day mean size at a given luminosity (upper panels), and the analogous ratio at a given mass (lower panels). The present-day values are derived from the SDSS sample (Shen et al. 2003). The comparison is restricted to the luminous ($L_v \gtrsim 3.4 \times 10^{10} h_{70}^{-2} L_\odot$) and to massive ($M_* \gtrsim 3 \times 10^{10} h_{70}^{-2} M_\odot$) galaxies. Open squares correspond to the GEMS sample (McIntosh et al. 2005; Barden et al. 2005) for galaxies with $z < 1$ and solid points indicate the results from FIRES. The star indicates our local reference values from SDSS (mean $z \sim 0.1$). We present the dispersion (dashed error bars) of the distribution and the uncertainty (2σ) at the mean determination (solid error bars). The open circles correspond to a 7% correction of the sizes to model the size bias found through a comparison with NICMOS data (see text for details). *Left column:* The dashed lines illustrate the expected evolution (Mo et al. 1998) at a fixed at fixed halo mass $R \propto H^{-2/3}(z)$ normalized to be 1 at $z=0.1$. The predicted size evolution at a given luminosity for Milky Way type objects (from the Bouwens & Silk 2002 infall model) is indicated with a solid line in the upper left panel. In the lower left panel we show (dotted line) the Mo et al. (1998) size evolution at a given halo mass corrected by the evolution of the stellar to halo mass $f_M(z) = (M_{\text{halo}}/M_*)^{1/3}(z)$. The solid line accounts for the transformation of the gas settled in the disk into stars by multiplying the above correction for an extra factor $f_S(z) = R_*/R_{\text{disk}}(z)$. *Right column:* Dashed lines illustrate the expected size evolution for single-age stellar population models with different formation redshift (computed assuming a Salpeter 1955 IMF using the PEGASE (Fioc & Rocca-Volmerange 1997) code).

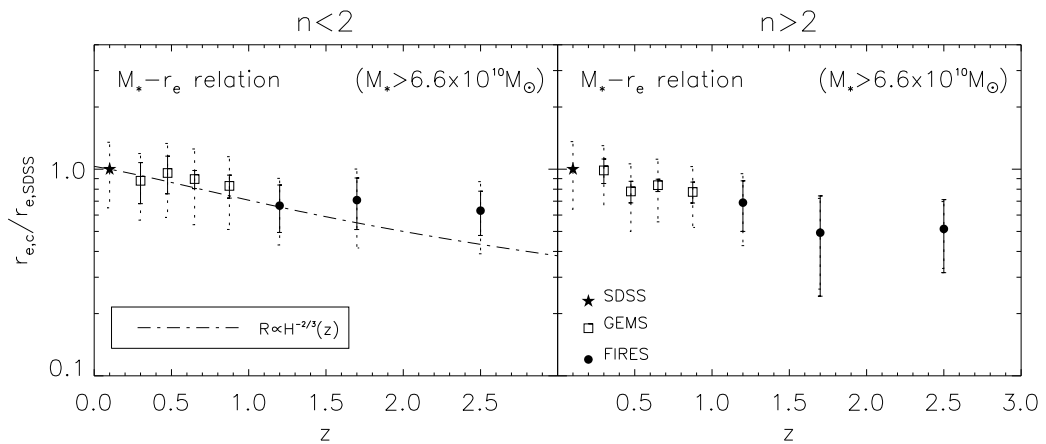


FIG. 13.— The ratio between observed size and expected size and at a given mass from the local SDSS sample (Shen et al. 2003) as a function of z for galaxies more massive than our completeness mass limit ($M_* \gtrsim 6.6 \times 10^{10} h_{70}^{-2} M_\odot$). The meaning of the symbols is the same than in Fig. 12. For the highly concentrated objects the size evolution seems to be critically dependent of the mass limit cut, pointing out to a tilt (see text for details) on the stellar mass-size distribution at high- z compared to the observed local relation.

$H^{-2/3}(z)$ result. This scaling is shown in the top left panel of Fig. 12, tantalizingly following the observations. Yet, it must be borne in mind that this match implies a mean stellar M/L that is constant with redshift, known to be incompatible with the color evolution of the same galaxies. The agreement between $H^{-2/3}(z)$ and the data must therefore be considered fortuitous, rather than a direct confirmation of the Mo et al. model.

The infall (Bouwens & Silk 2002) model predicts directly the evolution of the size at a given luminosity for Milky Way type objects. For that reason, we compare the infall model only with the observed size evolution at a given luminosity for galaxies with exponential-type profiles (first panel in Fig. 12). We see that the agreement of this model with the observed evolution is excellent for galaxies with $z < 1.7$. The infall model, however, shows an improbably fast decrease for galaxies with $z > 2.5$ and, for $z \gtrsim 3.7$, this model produces sizes with values less than zero.

If we focus now on the size evolution at a given disk mass and assume that the stellar mass is a good indicator of the total baryonic mass settled in the disk (which the gas fraction at high redshift might invalidate), we can make a comparison between the Mo et al. model prediction and the observed size evolution at a given disk mass. The bottom left panel of Fig. 12 shows that this hierarchical model (under the assumption stated in the Introduction) fails to describe the observations. The observed evolution is less strong than the predicted size evolution $R \propto H^{-2/3}(z)$ at a fixed halo mass.

The Mo et al. (1998) model describes the evolution the baryonic disk size at a given halo mass whereas the data show the stellar disk size evolution at a given stellar mass. We now explore whether this difference maybe responsible for the data model discrepancy apparent in the bottom left panel of Fig. 12. We consider two aspects: a) the ratio of stellar mass to halo mass, M_*/M_{halo} , can evolve with redshift and b) the ratio of the stellar disk to the baryonic disk size, R_*/R_{disk} , can also change.

These factors can be visualized by writing out the following identity:

$$\frac{R_*}{M_*^{1/3}}(z) = \frac{R_{disk}}{M_{halo}^{1/3}}(z) \times \left(\frac{M_{halo}}{M_*}(z) \right)^{1/3} \times \frac{R_*}{R_{disk}}(z) \quad (2)$$

where $R_*/M_*^{1/3}$ are the observables and $R_{disk}/M_{halo}^{1/3}$ are the quantities more immediately predicted by Mo et al. (1998).

One possible choice to describe the accumulation of stellar mass within halos is by the globally measured buildup of stellar mass: $M_*/M_{halo}(z) \sim <\rho_*(z)>$, where we take $<\rho_*(z)>$ from Rudnick et al. (2003). Taking $R_*/R_{disk} \equiv 1$ for now, this picture would predict a nearly redshift-independent R_*/M_* relation (dotted line in bottom left panel of Fig. 12), much closer to the observations. However, this picture would imply that stellar disk form from early-on in large halos and that the stellar disk, already in its infancy ($M_*/M_{halo} \ll M_*/M_{halo}(z=0)$) samples the full angular momentum distribution of its large halo.

From a variety of observational and theoretical arguments R_*/R_{disk} cannot be unity at all epochs. As the solid line in Fig. 12 illustrates, through altering this assumption by only 10–15% (i.e. by assuming $R_*/R_{disk}(z) \propto H^{-1/10}(z)$) it would be easy to match the observations.

The modest degree of evolution in the observed stellar mass–size relation with redshift implies that galaxies must evolve basically along this relation with time, increasing their

size as they build up their stellar mass. If galaxies on average were to increase their stellar mass without much changing their sizes, as implied by $R_*/R_{disk} \sim 1$, then the stellar mass–size would change more than observed. Instead, galaxies on average appear to grow inside–out "along" this relation. If this is the case, newly formed stars must preferentially reside at larger and larger radii, i.e. galaxies form from the inside out.

In interpreting the evolution of spheroid–like objects ($n > 2$) a different reference hypothesis suggests itself: we analyze whether the decrease in typical galaxy effective radius with lookback time at a given luminosity is consistent with a passively fading galaxy population.

To test the above idea we plot on Fig. 12 different tracks showing the expected size evolution of a fading galaxy population with different formation redshifts. These tracks are evaluated under the assumption that the shape of the local luminosity–size relation does not change with redshift but for a shift of the relation to brighter luminosities at increasing z . The increase in the luminosity with z is estimated by using the expected luminosity evolution from a single burst at high– z (in our case, we have used $z_{form} = 3, 5$ and 7) using the PÉGASE code (Fioc & Rocca–Volmerange 1997). Following the same procedure as with actual data, after shifting the luminosity–size relation we measure the ratio between the effective radii at a given luminosity for luminosities brighter than $3.4 \times 10^{10} h_{70}^{-2} L_\odot$.

The comparison between the actual data and the predicted tracks must be taken with caution: the better agreement with tracks with higher z_{form} (particularly at the higher redshift points) is probably caused by a progenitor bias (van Dokkum & Franx 2001). So, this high formation redshift must not be necessarily a characteristic of the galaxies in our sample for lower z .

Observationally, the result of this paper would be consistent with passive evolution of the observed spheroid–like objects since $z \sim 3$ if demonstrated that these galaxies are not creating new stars and just fading since that time. The answer to this point is beyond the scope of this paper but we plan to present a detailed analysis of this question in Zirm et al (2005). However, it seems unlikely that the full population of spheroid galaxies we see today were evolving passively since $z \sim 3$. In particular, the co–moving total stellar mass density in passive red–sequence galaxies is lower at earlier epochs, amounting to a factor of ~ 2 buildup since $z \sim 1$ (Chen et al. 2003; Bell et al. 2004; Cross et al. 2004) or a factor of ~ 10 since $z \sim 3$ (Labbé et al. 2005).

We want to add a final cautionary note on the interpretation of the evolution of the luminosity–size and stellar mass–size relations. There is a hint that the degree of evolution of these relations can be different depending of the luminosity and stellar mass range (or size) analyzed (Barden et al. 2005; McIntosh et al. 2005). In particular, we find that if we move the stellar mass limit to larger values than the current limit (i.e. if we select galaxies with values larger than $M_* \gtrsim 3 \times 10^{10} h_{70}^{-2} M_\odot$) the evolution in the sizes (at a given stellar mass) is larger than if we maintain the current limit. This implies a potential tilt of the stellar mass–size relation at higher– z , in the sense of being much flatter than is in the present day universe. The effect of this tilt in our results is illustrated in Fig. 13. There we show the size evolution for galaxies more massive than our completeness mass limit ($M_* \gtrsim 6.6 \times 10^{10} h_{70}^{-2} M_\odot$).

The disk-like objects size evolution is not strongly affected by this more conservative mass cut and the conclusions we have stated before are maintained but with larger uncertainties. However, for the spheroid-like objects the size evolution seems to be critically dependent on the mass limit cut. The number of objects that we have at the very high mass end is not enough to confirm that this tilt is real. However, Daddi et al. (2005) find 4 very compact ($r_e \lesssim 1$ kpc) and massive ($M_* \gtrsim 10^{11} h_{70}^{-2} M_\odot$) objects at $z \sim 1.7$ in the UDF supporting this view. These high- z spheroid-like objects are very massive so it is not expected that their masses can increase dramatically since then. So, we must expect a mechanism of growing in size very rapid at increasing their masses. As stated in the Introduction, the merger of early-type galaxies could increase their sizes. If this is the case, repeated mergers of the most massive spheroid-like objects that we observe at $z > 1.5$ could bring them into the local observed stellar mass-size relation of early-type galaxies.

7. SUMMARY

Using very deep near-infrared images of the HDF-S and the MS1054-03 field from the FIRES survey we have analyzed the evolution of the luminosity-size and stellar mass-size relation, measured in their optical rest-frame, for luminous ($L_V \gtrsim 3.4 \times 10^{10} h_{70}^{-2} L_\odot$) and massive ($M_* \gtrsim 3 \times 10^{10} h_{70}^{-2} M_\odot$) galaxies with $z > 1$. By combining HDF-S with the MS1054-03 field we have tripled the number of galaxies with $z > 1$ used in Trujillo et al. (2004).

Several tests have been run in order to estimate the robustness of our structural parameter estimates. From these tests we estimate an uncertainty in our sizes of $\sim 30\%$ and in the concentration (Sérsic index n) parameter of $\sim 50\%$. Moreover, we have analyzed whether our sample is affected by surface brightness selection effects. As shown in that analysis, our magnitude selection criterion is conservative enough to avoid such a concern.

Combining the analysis of FIRES data with the results obtained by GEMS at $z < 1$ (Barden et al. 2005; McIntosh et al. 2005) and tying both to the present-day results from SDSS (Shen et al. 2003) we trace a detailed picture of the evolution of the luminosity and stellar mass-size relations in the last ~ 11 Gyr. For disk-like objects ($n < 2$), at a given luminosity, the typical sizes of the galaxies were ~ 2.3 smaller at $z \sim 2.5$ than those we see today. In contrast, the stellar mass-size relation has evolved significantly less: we see very little evolution to $z \sim 1.2$ and a factor of ~ 1.5 decrease in size at a given stellar mass at $z \sim 2.5$. As pointed out by Trujillo et al. (2004) the different evolution in the luminosity-size and the stellar mass-size relation is explained by the fact that the M/L ratios of high- z galaxies are lower than nowadays (or, the stellar populations were much younger at earlier times). The modest evolution observed in the stellar mass-size relation combined with the fact that galaxies are producing new stars implies that galaxies evolve mainly along that relation. This points directly towards an inside-out growth of the galactic mass.

While the empirical results are quite clear and consistent, they do not fit easily in the context of existing hierarchical models of disk galaxy formation. The observed luminosity-size relation evolution out to $z \sim 1.7$ for disk-like objects

matches very well the expected evolution for Milky-Way type objects from infall models. But for disk-like galaxies, the semi-analytical hierarchical predictions based on simple scaling relations between halos and baryons do not reproduce the observed evolution of the stellar mass-size relation. The discrepancy is in the sense that the observed galaxies at high redshift are larger than expected from the model scalings. We have shown that qualitatively the discrepancy could be remedied if the high redshift disks already sit in large halos, where only a much smaller fraction of baryons have turned into stars sampling the halo's angular momentum. However, this picture also implies that within a given halo the baryon reservoir at early epochs, from which subsequent stars form, would have an angular momentum distribution that is barely larger ($R_*/R_{disk} \sim 1$); then it would be difficult for disks to grow inside-out. Hence the observed modest evolution of the M_* - R_* relation still awaits a satisfactory explanation in a hierarchical context.

For spheroid-like objects ($n > 2$), the evolution of the luminosity-size relation is consistent with (but does not necessarily imply) pure luminosity evolution of a fading galaxy population. Our observations are consistent with no evolution of the stellar mass-size relation for these objects although the uncertainties are large due to the limited number of galaxies. However, there is a hint that the most massive ($M_* \gtrsim 6.6 \times 10^{10} h_{70}^{-2} M_\odot$) spheroid-like objects at $z > 1.4$ in our sample were ~ 2 times smaller than equal mass present-day early-type galaxies.

We are happy to thank Shiyan Shen for providing us with the Sloan Digital Sky Survey data used in this paper, Eric F. Bell, E. Daddi and C. Heymans for useful discussions. We thank the staff at ESO for the assistance in obtaining the FIRES data and the Lorentz Center for its hospitality and support.

Funding for the creation and distribution of the SDSS Archive has been provided by the Alfred P. Sloan Foundation, the Participating Institutions, the National Aeronautics and Space Administration, the National Science Foundation, the US Department of Energy, the Japanese Monbukagakusho, and the Max-Planck Society. The SDSS Web site is <http://www.sdss.org>. The SDSS is managed by the Astrophysical Research Consortium (ARC) for the Participating Institutions. The Participating Institutions are the University of Chicago, Fermilab, the Institute for Advanced Study, the Japan Participation Group, Johns Hopkins University, Los Alamos National Laboratory, the Max-Planck-Institut für Astronomie (MPIA), the Max-Planck-Institut für Astrophysik (MPA), New Mexico State University, University of Pittsburgh, Princeton University, the US Naval Observatory, and the University of Washington.

GR acknowledges the support of a Goldberg fellowship at the National Optical Astronomy Observatory (NOAO), which is operated by the Association of Universities for Research in Astronomy (AURA), Inc., under a cooperative agreement with the National Science Foundation. GR also acknowledges the financial support of the Sonderforschungsbereich 375 Astroteilchenphysik. MB acknowledges support from the *Verbundforschung* of the BMBF.

REFERENCES

Barden, M. et al. 2005, ApJ, submitted, astro-ph/0502416
 Blanton, M. et al., 2003, ApJ, 592, 819
 Bell, E. F. & de Jong, R. S., 2001, ApJ, 550, 212

Bell, E. F., McIntosh, D.H., Katz, N., & Weinberg, M.D., 2003, ApJS, 149, 289
 Bell, E. F. et al., 2004, ApJ, 608, 752

Bertin, E., & Arnouts, S., 1996, A&AS, 117, 393

Bouwens, R. J., Cayón, L., & Silk, J. 1997, ApJ, 489, L21

Bouwens, R. J. & Silk, J. 2002, ApJ, 568, 522

Bouwens, R. J., Illingworth, G.D., Blakeslee, J. P., Broadhurst, T.J. & Franx, M., 2004, ApJ, 611, L1

Bruzual, G. & Charlot, S., 2003, MNRAS, 344, 1000

Casertano, S., Ratnatunga, K. U., Griffiths, R. E., Im, M., Neuschaefer, L. W., Ostrander, E. J. & Windhorst, R. A., 1995, ApJ, 453, 599

Casertano, S. et al. 2000, AJ, 122, 2205

Cayón, L., Silk, J. & Charlot, S. 1996, ApJ, 467, L53

Chen, H., et al. 2003, ApJ, 586, 745

Cross, N.J.G., et al., 2004, AJ, 128, 1990

Daddi, E., Cimatti, A., Renzini, A., Fontana, A., Mignoli, M., Pozzetti, L., Tozzi, P. & Zamorani, G., 2004, ApJ, 617, 746

Daddi, E. et al., 2005, ApJ, in press, astro-ph/0503102

Dalcanton, J.J., Spergel, D. N., James, J.E., Schmidt, M., & Schneider, D. P., 1997, AJ, 114, 635

Eggen, O. J., Lynden-Bell, D., & Sandage, A. R., 1962, ApJ, 136, 748

Fall, S. M. & Efstathiou, G., 1980, MNRAS, 193, 189

Fasano, G. & Franceschini, A., 1987, MNRAS, 225, 155

Ferguson et al. 2004, ApJ, 600, L107

Fioc, M., & Rocca-Volmerange, B., 1997, A&A, 326, 950

Förster Schreiber et al. 2004, ApJ, 616, 40

Förster Schreiber et al. 2005, in preparation

Franx, M. et al., "FIRES at the VLT: the Faint Infrared Extragalactic Survey", The Messenger 99, pp. 20–22, 2000

Franx, M. et al., 2003, ApJL, 587, L79

Giavalisco, M., Steidel C.C. & Macchetto, F.D., 1996, ApJ, 470, 189

Giavalisco, M., 2002, ARA&A, 40, 579

Hoekstra, H., Franx, M. & Kuijken, K., 2000, ApJ, 532, 88

Im M., Griffiths, R.E., Ratnatunga, K.U., & Sarajedini V.L. 1996, ApJ, 461, L79

Im M. et al., 2002, ApJ, 571, 136

Kauffmann, G., & Haehnelt, M., 311, 576

Kauffmann, G., et al., 2003, MNRAS, 341, 33

Khochfar, S. & Burkert, A., 2003, ApJ, 597, L117

Kroupa, P., 2001, MNRAS, 322, 231

Labbé, I.F.L. et al., 2003, AJ, 125, 1107

Labbé, I.F.L. et al., 2003b, ApJ, 591, L95

Labbé, I.F.L. et al., 2005, ApJ, in press

Larson, R., 1975, MNRAS, 173, 671

Lilly, S. et al. 1998, ApJ, 500, 75

Lowenthal, J.D., Koo, D.C., Guzmán, R., Gallego, J., Phillips, A.C., Faber, S.M., Vogt, N.P., Illingworth G.D., 1997, ApJ, 481, 67

McIntosh, D. H., et al. 2005, ApJ, submitted, astro-ph/0411772

Mo, H. J., Mao, S. & White, S.D.M., 1999, MNRAS, 304, 175

Moorwood, A. F. 1997, Proc. SPIE, 2871, 1146

Navarro, J., & Steinmetz, M. 2000, ApJ, 538, 477

Papovich, C., Dickinson, M., Giavalisco, M., Conselice, C.J. & Ferguson, H., 2005, ApJ, in press

Peng, C.Y., Ho, L.C., Impey, C.D. & Rix, H.W., 2002, AJ, 124, 266

Press, W.H., Teukolsky, S.A., Vetterling, W.T. & Flannery, B.P., 1992, Numerical Recipes (Cambridge: Cambridge Univ. Press)

Ravindranath, S. et al. 2004, ApJ, 604, L9

Rix, H.-W. et al., 2004, ApJS, 152, 163

Roche, N., Ratnatunga, K., Griffiths, R. E., Im, M. & Naim, A., 1998, MNRAS, 293, 157

Rudnick, G. et al., 2001, AJ, 122, 2205

Rudnick, G. et al., 2003, ApJ, 599, 847

Rudnick, G. et al., 2005, in preparation

Salpeter, E.E., 1955, ApJ, 121, 161

Schade D. et al. 1999, ApJ, 525, 31

Sérsic, J.-L. 1968, Atlas de Galaxias Australes (Cordoba: Observatorio Astronomico)

Shen, S., Mo, H.J., White, S.D.M., Blanton, M.R., Kauffmann, G., Voges, W., Brinkmann, J. & Csabai, I., MNRAS, 2003, 343, 978

Smail, I., Hogg, D. W., Yan, L., Cohen, J. G., 1995, ApJ, 449, L105

Simard, L., 1998, Astronomical Data Analysis Software and Systems VII, A.S.P. Conference Series, Vol. 145, 1998, R. Albrecht, R.N. Hook and H.A. Bushouse, eds., p.108

Simard, L., et al. 1999, ApJ, 519, 563

Steidel C.C., Giavalisco, M., Pettini, M., Dickinson, M., & Adelberger, K. L., 1996, ApJ, 462, L17

Trujillo, I. et al., 2004, ApJ, 604, 521

Trujillo, I. & Aguerri, J. A. L., 2004, MNRAS, 355, 82

van den Bosch, F. C., 2000, ApJ, 530, 177

van Dokkum, P.G., Franx, M., Fabricant, D., Illingworth, G.D., & Kelson, D.D., 2000, ApJ, 541, 95

van Dokkum, P.G. & Franx, M., 2001, ApJ, 553, 90

van Dokkum, P.G. et al. 2003, ApJ, 587, L53

van Dokkum, P.G. et al. 2004, ApJ, 611, 703

Vogt N. P., Forbes, D. A., Phillips, A. C., Gronwall, C., Faber, S. M., Illingworth, G. D., Koo, D. C., 1996, ApJ, 465, L15

Vogt N. P. et al. 1997, 1997, ApJ, 479, L121

White, S.D.M., Frenk, C. S., 1991, 379, 52

Wolf C. et al., 2001, A&A, 365, 681

Wolf C., Meisenheimer, K., Rix, H.W., Borch, A., Dye, S., Kleinheinrich, M., 2003, A&A, 401, 73

York D. et al., 2000, AJ, 120, 1579

Zirm A. et al., 2005, in preparation

TABLE 4
 PROPERTIES OF THE MS1054-03 SAMPLE GALAXIES

Galaxy	$K_{s,tot}$	r_e	n	ϵ	$L_V(10^{10} h_{70}^{-2} L_\odot)$	$M(10^{10} h_{70}^{-2} M_\odot)$	z	Filter
355	21.76	0.90	1.02	0.42	1.37	2.92	1.020	J_s
1258	20.48	0.25	1.58	0.21	4.34	21.46	1.020	J_s
848	22.01	0.66	1.08	0.53	1.13	1.76	1.040	J_s
1638	22.64	0.34	7.56	0.05	0.54	1.56	1.040	J_s
1055	22.59	0.57	1.24	0.30	0.60	1.82	1.060	J_s
1132	20.87	0.57	1.21	0.45	2.51	9.02	1.060a	J_s
1434	21.93	0.33	1.91	0.26	1.55	2.84	1.060	J_s
1566	21.78	0.53	0.81	0.41	1.01	3.65	1.060a	J_s
1575	22.41	0.34	0.65	0.25	1.53	1.08	1.060a	J_s
1801	21.36	0.17	1.80	0.05	2.43	7.70	1.070a	J_s
830	22.29	0.36	1.03	0.35	1.50	1.22	1.073a	J_s
1401	20.41	0.52	1.33	0.33	8.67	4.52	1.074a	J_s
714	20.70	0.51	0.71	0.31	3.21	7.39	1.076a	J_s
178	22.25	0.51	0.86	0.49	2.10	1.20	1.080	J_s
862	22.53	0.79	0.27	0.60	0.62	1.30	1.080	J_s
1229	22.78	0.45	1.51	0.20	1.37	1.37	1.080	J_s
1497	22.65	0.51	0.79	0.54	1.42	1.14	1.080	J_s
617	20.68	0.92	1.54	0.40	4.42	19.59	1.100	J_s
147	22.33	0.37	0.54	0.28	1.38	2.39	1.120	J_s
150	22.55	0.32	1.00	0.06	1.54	2.54	1.120	J_s
359	22.59	0.97	0.97	0.63	1.38	1.06	1.120	J_s
1216	21.29	0.22	3.75	0.28	2.69	15.27	1.120	J_s
1768	21.28	0.59	1.15	0.42	2.50	7.41	1.120	J_s
460	22.31	0.49	0.49	0.35	2.15	1.13	1.139a	J_s
100	21.13	0.28	1.74	0.30	3.08	15.69	1.140	J_s
527	21.02	0.60	3.91	0.18	3.35	16.32	1.140	J_s
749	21.15	0.47	3.63	0.25	3.73	9.72	1.140	J_s
1172	22.50	0.28	3.92	0.10	0.91	6.68	1.140	J_s
1440	22.18	0.53	0.72	0.40	2.43	2.75	1.160	J_s
1785	20.05	0.57	1.21	0.40	11.31	32.57	1.170a	J_s
494	21.87	0.29	3.44	0.18	2.43	3.14	1.174a	J_s
481	21.81	0.40	4.42	0.67	1.89	7.74	1.180	J_s
1273	22.15	0.21	0.61	0.11	2.11	1.82	1.180	J_s
1535	21.75	0.68	0.59	0.37	1.77	0.97	1.181a	J_s
508	21.49	1.47	1.53	0.82	1.60	5.75	1.189a	J_s
161	20.44	0.16	7.31	0.05	7.37	7.30	1.200	J_s
1301	21.91	0.27	2.84	0.19	1.82	30.93	1.200	J_s
1786	21.46	0.28	4.00	0.07	2.81	25.32	1.200	J_s
45	22.36	0.66	1.09	0.38	2.07	1.73	1.220	J_s
306	20.90	0.84	1.02	0.09	6.65	5.47	1.220	J_s
614	20.75	0.55	2.48	0.49	5.25	11.28	1.220	J_s
1621	21.85	0.61	0.32	0.45	2.50	4.93	1.220	J_s
441	20.52	0.56	2.35	0.32	6.88	17.65	1.230a	J_s
1176	22.88	0.30	1.25	0.21	1.60	0.84	1.234a	J_s
743	22.48	0.26	1.07	0.25	1.11	5.87	1.240	J_s
774	21.97	0.65	0.96	0.50	3.03	3.35	1.240	J_s
1474	21.93	0.77	0.80	0.26	3.71	2.55	1.245a	J_s
1267	22.45	0.43	1.11	0.42	0.91	0.53	1.245a	J_s
1438	21.71	0.73	1.49	0.49	3.23	3.43	1.247a	J_s
737	21.09	0.63	1.33	0.49	6.08	9.30	1.280	J_s
1266	22.34	0.41	0.80	0.38	1.63	2.94	1.280	J_s
1280	22.05	0.32	4.38	0.42	2.94	3.74	1.280	J_s
1226	22.87	0.44	0.90	0.31	1.64	0.78	1.295a	J_s
54	21.78	0.69	0.90	0.36	3.60	3.94	1.300	J_s
487	22.51	2.62	0.93	0.83	1.09	1.77	1.300	J_s
869	22.51	0.25	0.20	0.20	1.83	1.96	1.300	J_s
971	22.98	0.37	2.68	0.60	0.93	1.52	1.300	J_s
1256	20.50	0.54	1.42	0.15	10.29	22.84	1.300	J_s
1637	21.77	1.34	0.84	0.81	1.89	3.51	1.300a	J_s
1071	21.52	0.28	3.00	0.25	3.49	16.61	1.320	J_s
1456	21.58	0.22	3.93	0.08	5.35	2.76	1.320	J_s
438	22.17	0.59	1.74	0.05	3.30	2.03	1.320a	J_s
67	21.06	0.70	3.35	0.20	7.06	6.20	1.325a	J_s
479	22.60	0.50	1.06	0.60	1.60	1.86	1.340	J_s
1120	22.68	0.60	0.31	0.41	2.08	1.02	1.340	J_s
1218	22.21	1.06	0.83	0.71	3.17	2.53	1.340	J_s
732	22.61	0.78	1.33	0.22	1.93	1.11	1.360	J_s
795	21.68	0.73	0.46	0.31	3.00	8.46	1.360	J_s
845	21.79	0.57	0.66	0.25	4.46	2.87	1.360	J_s
1719	20.79	0.50	2.34	0.27	7.73	18.69	1.400a	J_s
1763	22.17	0.37	1.51	0.25	2.89	4.02	1.400	J_s
1781	21.21	0.31	4.00	0.07	4.94	28.18	1.400	J_s
379	22.80	0.97	1.34	0.59	1.90	1.42	1.420	J_s
552	22.32	0.60	0.52	0.56	2.48	3.08	1.420	J_s
1249	22.53	0.85	0.56	0.58	2.71	2.26	1.420	J_s

TABLE 4 — *Continued*

Galaxy	$K_{s,tot}$	r_e	n	ϵ	$L_V(10^{10} h_{70}^{-2} L_\odot)$	$M(10^{10} h_{70}^{-2} M_\odot)$	z	Filter
40	22.20	0.62	0.34	0.54	1.84	4.36	1.440	J_s
259	22.93	0.36	1.01	0.31	1.96	1.16	1.460	J_s
831	22.17	0.97	0.43	0.52	4.78	4.54	1.460	J_s
878	22.46	0.31	1.49	0.30	3.18	1.63	1.460	J_s
1341	22.51	0.39	0.77	0.26	2.29	2.79	1.460	J_s
1792	22.10	0.79	0.50	0.56	2.28	8.60	1.460	J_s
706	22.81	0.48	0.36	0.32	1.45	1.54	1.480	J_s
1378	22.90	0.41	0.88	0.38	2.11	1.06	1.480	J_s
1292	22.84	0.28	1.11	0.10	2.43	2.00	1.500	H
999	22.69	0.35	4.61	0.10	1.49	5.43	1.520	H
1671	21.28	0.65	1.68	0.30	7.01	10.69	1.520	H
321	22.20	0.31	1.73	0.05	3.12	3.93	1.540	H
1268	22.80	0.49	0.34	0.38	2.57	2.55	1.540	H
1591	22.15	0.31	1.19	0.20	4.68	4.05	1.540	H
1155	21.87	0.43	1.39	0.35	4.06	10.08	1.560	H
1124	22.61	0.67	0.74	0.69	2.65	3.46	1.580	H
37	21.06	0.22	1.08	0.10	10.27	24.11	1.600	H
1540	21.75	0.21	1.82	0.29	4.61	14.09	1.600	H
1704	21.50	0.79	0.44	0.62	8.02	7.44	1.600	H
1774	21.60	0.13	3.21	0.10	5.66	25.10	1.600	H
1797	21.82	0.19	4.02	0.23	4.06	28.02	1.600	H
807	22.99	0.41	0.61	0.45	2.58	2.67	1.620	H
928	21.19	0.47	1.68	0.50	9.05	31.61	1.620	H
110	22.84	0.38	4.00	0.40	2.48	1.66	1.640	H
281	22.63	0.61	0.91	0.40	3.87	2.62	1.640	H
582	22.92	0.19	1.02	0.14	2.82	1.97	1.640	H
962	22.16	0.19	2.56	0.23	3.63	5.58	1.640	H
1199	22.39	0.26	0.47	0.15	3.56	2.55	1.640	H
1586	21.89	0.34	2.62	0.10	5.35	7.26	1.640	H
1753	22.86	0.53	4.00	0.39	1.70	3.95	1.640	H
157	22.86	0.50	0.72	0.38	2.19	1.51	1.660	H
1577	22.30	0.19	1.10	0.25	4.29	6.05	1.660	H
1695	21.98	0.68	1.07	0.20	4.50	8.76	1.660	H
1776	22.03	0.49	0.30	0.31	4.75	8.12	1.660	H
402	22.62	0.22	1.11	0.10	3.68	1.88	1.700	H
523	22.33	0.24	0.31	0.10	3.06	12.26	1.700	H
528	20.32	0.33	2.29	0.22	24.52	39.41	1.700a	H
561	20.39	0.43	2.25	0.46	21.70	38.66	1.700a	H
713	20.46	0.40	3.17	0.18	20.55	38.82	1.700a	H
1350	22.01	0.88	1.61	0.40	4.84	3.81	1.700	H
1295	21.55	0.34	2.60	0.19	7.21	17.20	1.720	H
1459	21.32	0.37	4.52	0.46	7.43	21.36	1.740	H
1309	22.90	0.28	0.95	0.20	2.16	8.66	1.800	H
73	21.80	0.10	1.97	0.25	6.14	25.09	1.820	H
1650	22.96	0.38	2.44	0.10	2.94	3.03	1.820	H
7	22.44	0.30	0.50	0.19	3.62	24.70	1.860	H
1717	22.62	0.14	1.90	0.88	3.46	6.66	1.860	H
723	21.32	0.71	0.98	0.31	9.78	52.79	1.880	H
1714	21.47	0.95	1.56	0.52	8.97	23.26	1.880	H
842	22.78	0.38	2.08	0.10	4.11	3.56	1.900	H
386	22.88	0.35	0.69	0.44	2.18	5.98	1.920	H
1530	22.73	0.41	0.59	0.33	4.13	2.70	1.920	H
1702	22.56	1.42	0.60	0.72	4.57	2.43	1.940	H
1373	22.07	0.64	1.04	0.20	6.68	5.73	1.960	H
926	22.18	0.83	0.28	0.57	4.43	17.94	1.980	H
1335	22.97	0.35	1.00	0.10	2.50	13.06	1.980	H
1294	22.51	0.42	0.49	0.30	5.11	6.86	2.000	H
1457	22.85	0.56	0.62	0.38	2.85	3.49	2.000	H
1571	21.78	0.38	0.66	0.35	9.22	6.27	2.020	H
1061	21.48	0.42	2.26	0.20	11.54	62.24	2.120	H
325	22.77	0.50	1.24	0.44	4.78	2.41	2.140	H
1265	22.06	0.11	3.83	0.18	9.48	13.54	2.140	H
1550	22.81	0.34	0.87	0.25	4.10	5.15	2.140	H
914	21.67	0.11	4.51	0.00	12.82	28.78	2.160	H
383	21.28	0.82	0.47	0.41	18.80	17.24	2.180	H
852	22.80	0.47	0.33	0.21	3.85	10.00	2.180	H
972	22.62	0.44	0.38	0.45	5.06	4.94	2.200	H
1644	22.71	0.40	0.53	0.29	4.26	9.16	2.200	H
1144	22.56	0.12	0.18	0.24	4.76	23.60	2.220	H
847	22.18	0.37	1.03	0.36	6.73	26.59	2.240	H
1612	22.01	0.45	0.70	0.43	8.93	38.78	2.240	H
1538	22.98	0.55	0.29	0.06	3.79	8.27	2.300	H
846	22.40	0.72	1.00	0.52	7.52	9.94	2.320	H
1086	22.56	0.22	0.57	0.22	7.10	3.37	2.340	H
1410	22.17	0.11	1.70	0.25	11.23	10.65	2.400	H
1035	21.43	0.30	3.00	0.19	19.64	13.72	2.425a	H

TABLE 4 — *Continued*

Galaxy	$K_{s,tot}$	r_e	n	ϵ	$L_V(10^{10} h_{70}^{-2} L_\odot)$	$M(10^{10} h_{70}^{-2} M_\odot)$	z	Filter
1356	21.53	0.06	4.29	0.06	18.50	25.46	2.427a	H
1383	21.41	0.74	1.79	0.36	18.45	61.06	2.430a	H
1547	22.51	0.56	5.52	0.43	8.15	13.51	2.480	H
1656	22.40	0.54	1.09	0.50	10.04	2.65	2.500	H
645	21.52	0.64	1.40	0.45	22.60	24.37	2.520	H
1239	22.70	0.26	0.6	0.14	8.89	3.96	2.620	K_s
1496	22.93	0.22	2.3	0.33	7.87	4.64	2.700	K_s
1237	22.97	0.35	1.7	0.12	7.26	9.70	2.760	K_s
773	22.85	0.24	2.03	0.10	8.72	2.96	2.800	K_s
1353	22.75	0.81	2.0	0.42	9.62	11.76	2.840	K_s
1100	22.50	1.50	1.1	0.51	12.33	18.50	2.880	K_s
1253	22.05	0.48	0.6	0.06	21.36	18.77	3.000	K_s
1041	22.72	0.53	5.6	0.10	14.09	11.44	3.480	K_s
1666	22.78	0.92	1.2	0.40	13.86	10.82	3.540	K_s
1211	22.82	0.77	1.2	0.59	15.84	8.26	3.780	K_s
543	22.84	0.48	2.7	0.10	24.24	9.39	4.760	K_s
549	22.27	0.36	2.3	0.10	58.93	29.30	4.900	K_s
472	22.65	0.21	2.4	0.13	38.90	17.49	4.960	K_s
859	22.50	0.54	2.4	0.23	61.63	31.61	5.200	K_s
1690	22.77	0.65	0.4	0.43	135.90	257.24	5.400	K_s
1758	22.11	0.33	0.9	0.36	287.53	450.87	5.740	K_s
1467	22.87	0.15	0.8	0.15	51.66	27.29	5.960	K_s
6	22.52	0.85	0.7	0.60	320.89	637.74	6.000	K_s
1778	22.72	0.51	3.1	0.30	73.47	45.16	6.000	K_s

NOTE. — Col. (1): Catalog identification numbers (see Förster Schreiber et al. 2005). Col (2): K_s -band total magnitudes. Col. (3): Semimajor axis optical restframe half-light radii (arcsec). The typical uncertainty on the size determination is 30%. Col. (4): Sérsic index n . The typical uncertainty on the shape determination is 50%. Col (5): intrinsic (i.e. the recovered non-seeing affected) ellipticity. Col (6): Rest-frame V-band luminosity. The typical uncertainty on the luminosity determination is 30%. Col (7): Stellar mass. Col (8): redshift (the index a mean spectroscopic z). Col (9): Filter used to measure the size of the galaxies